Quantitative Thermal Imaging of Single-Walled Carbon Nanotube Devices by Scanning Joule Expansion Microscopy

Xu Xie,[†] Kyle L. Grosse,[‡] Jizhou Song,[§] Chaofeng Lu,[⊥] Simon Dunham,[†] Frank Du,[†] Ahmad E. Islam,[†] Yuhang Li,[¶] Yihui Zhang,[¶,◇] Eric Pop,[∥] Yonggang Huang,[¶] William P. King,[‡,*] and John A. Rogers[†,‡,*]

[†]Department of Materials Science and Engineering and Frederick Seitz Materials Research Laboratory and [‡]Department of Mechanical Science and Engineering, University of Illinois at Urbana—Champaign, Urbana, Illinois 61801, United States, [§]Department of Mechanical and Aerospace Engineering, University of Miami, Coral Gables, Florida 33146, United States, [⊥]Department of Civil Engineering and Soft Matter Research Center, Zhejiang University, Hangzhou 310058, China, [∥]Department of Electrical and Computer Engineering and Micro and Nanotechnology Laboratory, University of Illinois at Urbana—Champaign, Urbana, Illinois 61801, United States, [¶]Department of Mechanical Engineering and Department of Civil and Environmental Engineering, Northwestern University, Evanston, Illinois 60208, United States, and [◇]Center for Mechanics and Materials, Tsinghua University, Beijing 100084, People's Republic of China

ABSTRACT Electrical generation of heat in single-walled carbon nanotubes (SWNTs) and subsequent thermal transport into the surroundings can critically affect the design, operation, and reliability of electronic and optoelectronic devices based on these materials. Here we investigate such heat generation and transport characteristics in perfectly aligned, horizontal arrays of SWNTs integrated into transistor structures. We present quantitative assessments of local thermometry at individual SWNTs in these arrays, evaluated using scanning Joule expansion microscopy. Measurements at different applied voltages reveal electronic behaviors, including metallic and semiconducting responses, spatial variations in diameter or chirality, and localized defect sites. Analytical models, validated by measurements performed on different device structures at various conditions, enable accurate, quantitative extraction of temperature distributions at the level of individual SWNTs. Using current equipment, the spatial resolution and temperature precision are as good as ~100 nm and ~0.7 K, respectively.

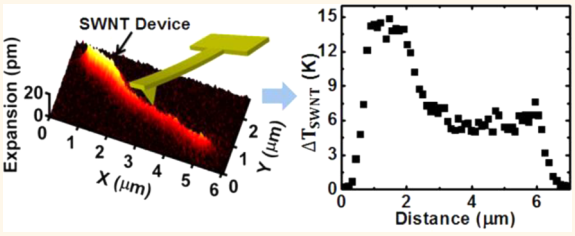

KEYWORDS: single-walled carbon nanotube · scanning Joule expansion microscopy · thermal expansion · heat generation · temperature distribution · resolution · chirality change · defect

Superior electrical and thermal properties of single-walled carbon nanotubes (SWNTs) enable high-performance transistors,[1,2] advanced interconnects,[3] and other components of relevance to various existing and emerging forms of electronics. Heat generation and transport characteristics of devices that incorporate SWNTs are critical in understanding the fundamental properties and engineering considerations in device design. Such issues are particularly important because all known growth techniques yield SWNTs with distributions in diameters and chiralities and with densities of defects that can affect device performance[4,5] either directly or indirectly through non-uniform distributions of Joule heating.[6,7] Although optical techniques, such as Raman[8−10] and infrared spectroscopy,[11,12] can map the distributions of temperature in SWNT devices, their limits in spatial and temperature resolution are defined by wavelengths of visible and infrared light and by background noise in the sensors, respectively. Methods based on atomic force microscopy (AFM), on the other hand, have the potential to overcome such limitations, thereby enabling studies of thermal transport at significantly improved resolution. One such technique, known as scanning thermal microscopy (SThM), offers useful capabilities in characterizing temperature distributions in nanometer-scale electronic devices.[13−17] In SThM, a specialized tip or cantilever incorporates an integrated temperature sensor that can be scanned over a surface to measure temperature with submicrometer spatial resolution.[17−21] Key challenges for SThM

* Address correspondence to jrogers@uiuc.edu, wpk@illinois.edu.

Received for review September 4, 2012 and accepted October 12, 2012.

Published online October 12, 2012
10.1021/nn304083a

are in integration and calibration of the required, specialized thermal probes. In particular, heat flow between the cantilever and substrate can be difficult to describe accurately, thereby diminishing the quantitative capabilities of the measurements.[22,23] Strategies for reducing these artifacts include extensive modeling, methods to subtract the background signals, and use of vacuum conditions during measurement.[22−24] Scanning Joule expansion microscopy (SJEM)[25,26] offers an alternative that avoids these challenges in which conventional AFM cantilevers measure nanometer-scale thermal expansions as a means to reveal underlying distributions of temperature.

Here we report the application and further development of the SJEM method to investigate heat generation and transport in transistors that incorporate straight, horizontally aligned arrays of individual SWNTs. The small dimensions (diameters ~0.5−1.7 nm)[27] of these SWNT-based heat sources and their quasi-one-dimensional nature differentiate them from structures that have been examined previously by SJEM.[28−30] The images directly and immediately reveal important physics associated with Joule heating in SWNT devices under various electrical bias conditions, in ways that can be used to identify defects and other nonideal features of the SWNTs, as well as variations in electrical switching behaviors. Quantitative interpretation of the results with analytical models and finite element analysis (FEA) for heat flow and thermal expansion enables accurate determination of the distributions in temperature. Studies using different device structures, examined at various operating frequencies, provide insights into the limits in spatial and temperature resolution and the important mechanics that govern interactions between the tip and sample. The results demonstrate that SJEM can be a useful tool for exploring thermal and electrical properties in SWNT devices and, by extension, other components that incorporate nanomaterials.

RESULTS AND DISCUSSION

Figure 1 shows a schematic illustration of the setup for SJEM measurement on a device with several straight, well-separated, aligned SWNTs on a SiO_2/Si substrate. An alternating voltage $V(t) = V_{ds}\cos(2\pi ft)$ applied between the drain and source contacts causes Joule heating in the SWNTs and an associated time-oscillating rise in temperature (with frequency $2f$). A direct current (DC) voltage applied to the silicon wafer serves as a back gate to control the electrostatics. A layer of poly(methyl methacrylate) (PMMA) spin-cast uniformly onto the device substrate protects the SWNTs during contact scanning and prevents electronic coupling between the tip and the device components. This film also amplifies the thermo-mechanical deformations (oscillating at $2f$) induced by thermal expansion that follow heat flow into the surroundings from the SWNT.[26] An AFM probe

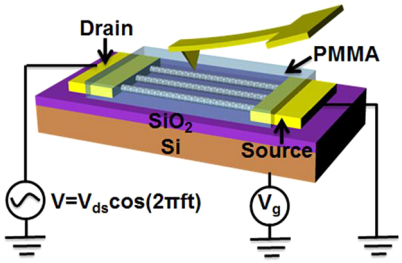

Figure 1. Schematic illustration of the experimental setup for scanning Joule expansion microscopy (SJEM) imaging of a SWNT device that incorporates several parallel, aligned tubes. The device consists of three terminals: two metal pads that contact the SWNTs to serve as the drain (alternating voltage) and source (grounded), and a third (doped silicon substrate) that serves as a gate. A layer of poly(methyl methacrylate) (PMMA) covers the device to protect the SWNTs and amplify the thermo-mechanical expansion caused by the Joule heating. An AFM probe operating in contact mode detects this expansion.

operating in contact mode and scanning the top surface of the PMMA measures the vertical displacements. Detection with a lock-in amplifier set to the frequency $2f$ reveals deflections of the AFM cantilever due to electrically driven thermal expansion. (Details of the SJEM setup appear in the Supporting Information, part 1 and Figure S1.) The two-dimensional (2D) spatial maps of thermo-mechanical expansion (*i.e.*, amplitude of the oscillating vertical displacement) that emerge from measurements of this sort are directly related to the heat generation in the SWNTs and thermal diffusion and, as a result, the associated temperature distributions.[25] Figure 1 corresponds to the case of SWNTs incorporated into a field effect transistor (FET) in a back-gated geometry, where the gate bias is V_g.

The arrays contain a mixture of metallic and semiconducting SWNTs. Figure 2a shows an AFM topographical map of a device with channel length $L \sim 3.7\ \mu$m that incorporates two SWNTs spaced by ~1.5 μm on a SiO_2/Si (300 nm/300 μm) substrate, with the drain and source contacts on the left and right, respectively. The device is coated with a layer of PMMA (thickness ~310 nm) for imaging. Figure 2b−f presents SJEM images collected at $f = 25$ kHz, $V_{ds} = 3$ V and at gate voltages of $V_g = 20, 10, 0, -10$, and -20 V, respectively. The expansion signals coincide with the locations of the SWNTs, for which maxima and minima occur in the channel and near the metal contacts, respectively, as would be expected based on heat flow considerations and operation of the device in the long-channel, diffusive transport regime.[6,15,31] For the SWNT in the upper region of this image, the expansion is similar for all gate voltages. By contrast, the SWNT in the lower region shows expansion that is nearly undetectable at $V_g = 20$ V but which gradually increases as V_g decreases and then becomes more negative. The expansion profiles along the upper and lower SWNTs appear in Figure 2g,h, respectively, for all V_g. The behaviors observed for the upper SWNT (Figure 2g) are consistent

with a metallic type and with heat flow into the substrate along the length of the SWNT and into the metal electrodes near the contacts, similar to previous observations.[7,14,15] Features observed for the lower SWNT are consistent with semiconducting behavior and hole transport. The maximum expansion signal at $V_g = -20$ V is about 10 times larger than that at $V_g = 20$ V, the latter of which is comparable to the noise level in the measurement. More interestingly, the shapes of the profiles change somewhat with V_g, suggesting variations of power dissipation along the SWNT during the switching process, presumably caused by some combination of electrostatics, charge transport in the SWNTs, and variations in local charge distributions, many aspects of which are influenced by time-dependent levels of hysteresis that are present in devices of this sort.[32]

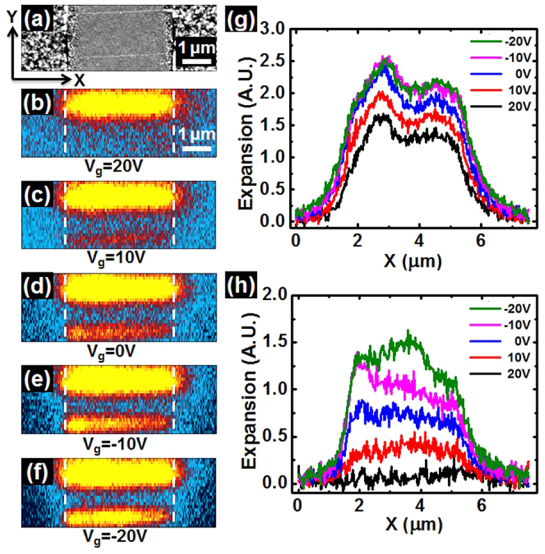

Figure 2. (a) Topographical AFM image of two SWNTs in the same FET. (b–f) SJEM images of the SWNTs at different gate voltages: V_g = (b) 20 V, (c) 10 V, (d) 0 V, (e) −10 V, and (f) −20 V. These images used V_{ds} = 3 V, f = 25 kHz, and PMMA thickness ∼310 nm. The white dashed lines indicate the edges of the metal contacts. (g,h) Thermo-mechanical expansion profiles along the two SWNTs at different V_g extracted from (b–f). The magnitudes and shapes of the expansion profiles from the upper SWNT do not change substantially with V_g (g), indicating metallic behavior; those from the lower SWNT show substantial changes with V_g (h), consistent with p-doped semiconducting behavior.

In addition to basic information such as identification of metallic and semiconducting behaviors, SJEM can reveal other electrical properties associated with heat dissipation. For example, Figure 3a shows a representative transfer characteristic and a scanning electron microscope (SEM) image (inset) of a device incorporating a single metallic SWNT formed by direct growth on a SiO_2/Si (200 nm/500 μm) substrate (see Methods). Figure 3b presents an SJEM image for V_{ds} = 3 V, V_g = 0 V, f = 30 kHz and with a PMMA coating thickness of ∼120 nm. Two distinct segments with substantially different expansion signals appear along the length of the SWNT. A close examination (Figure 3c) of the device, without the PMMA, reveals that the direction of the SWNT changes abruptly along the channel at the point that coincides with the change in thermal behaviors. AFM measurements of diameters yield 1.0(±0.25) and 1.2(±0.25) nm for the hotter and colder segments, respectively. These observations suggest that a change in chirality and diameter, which can occur during the growth,[33] results in different electrical resistances and power dissipation characteristics. Application of V_{ds} without the PMMA coating leads to the

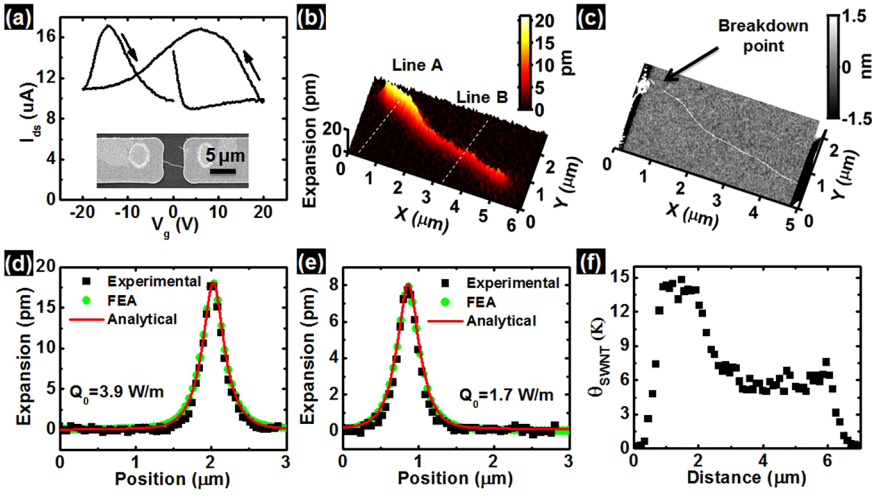

Figure 3. (a) Transfer curve of a single SWNT measured at V_{ds} = 3 V (DC voltage); the response indicates metallic behavior. The inset shows a scanning electron microscope (SEM) image of the device. (b) SJEM image of the same device, collected with V_{ds} = 3 V, f = 30 kHz, and PMMA thickness ∼120 nm. (c) Topographical AFM image of the SWNT collected after removing the PMMA and operating the device at high bias in air. The location of degradation (breakdown point) coincides with that of the highest thermal expansion signal. (d,e) Expansion signal profiles (black solid square) along the cross sections marked by dotted lines A and B in (b), respectively. Green solid circles and red lines represent results from 2D FEA and analytical models, respectively, in which the power density, Q_0, serves as a fitting parameter: Q_0 = 3.9 μW/μm for line A and Q_0 = 1.7 μW/μm for line B. (f) Calculated temperature distribution along the SWNT based on the SJEM measurement.

destruction of the SWNT to form a small gap (black arrow) that matches the location of the largest expansion signal, as might be expected for a thermally driven breakdown process.[6,31]

SJEM yields quantitative information about the power dissipation and temperature field that provides further insights into the physics of SWNT devices. Experimental demonstration of these capabilities is most clearly accomplished through SJEM measurements on devices that incorporate single, individual SWNTs, such as the one in Figure 3a. Figure 3d,e shows the expansion signal profiles (solid squares) for this device, extracted along cross sections marked by dotted lines A and B in Figure 3b, respectively. To quantitatively explain these profiles, we performed a 2D analytical study as well as a finite element analysis (FEA) of the coupled thermal and mechanical responses. Here a 2D treatment, for locations away from the contacts, represents a reasonable approximation due to the long lengths and small diameters (*i.e.*, large aspect ratio) of the SWNTs (see Supporting Information part 5 for the validation of the 2D models). Moreover, the typical thermal transfer length along the SWNT near the contacts is a few hundred nanometers,[6,31] which is much smaller than the overall length of the SWNT.

The analytically modeled system in this case includes a PMMA coating with thickness h_0 on a layer of SiO_2 with thickness h_1. The silicon substrate underneath is assumed to be infinite. The SWNT has radius r_0 and lies at the interface between the PMMA and SiO_2. The center of the SWNT marks the origin of a Cartesian coordinate system with x along the interface, in a direction perpendicular to the SWNT, and with y into the Si substrate (see Supporting Information, Figure S2). The temperature distribution is obtained by solving the heat diffusion equation

$$\frac{\partial\theta}{\partial t} - \alpha\left(\frac{\partial^2\theta}{\partial x^2} + \frac{\partial^2\theta}{\partial y^2}\right) = 0 \qquad (1)$$

where α is the thermal diffusivity and $\theta = T - T_\infty$ is the increase in temperature relative to the ambient temperature T_∞. In the following, subscripts 0, 1, and 2 specify the physical properties of the PMMA, SiO_2, and Si, respectively. The boundary conditions include zero heat flux at the top surface of the PMMA ($-k_0(\partial\theta/\partial y)|_{y=-h_0} = 0$, where k is the thermal conductivity) and ambient temperature at infinity ($\theta|_{y=\infty} = 0$). The temperatures and heat fluxes across all interfaces are assumed to be continuous, except at the location of the SWNT, where the heat generation requires $k_0(\partial\theta/\partial y)|_{y=0^-} - k_1(\partial\theta/\partial y)|_{y=0^+} = Q/\pi r_0$ for $|x| \le \pi r_0/2$, where Q is the power dissipation per unit length along the SWNT. For an applied voltage $V = V_{ds}\cos(\omega t)$ as in the experiments, $Q = Q_0(1 + \cos(2\omega t))$ has both DC (*i.e.*, Q_0) and AC (*i.e.*, $Q_0\cos(2\omega t)$) components, where $\omega = 2\pi f$ is the angular frequency and Q_0 is the amplitude of the oscillating power density. The resulting temperature rise and the thermal expansion will have both steady-state terms and time oscillating terms. Since SJEM measures the time-oscillating component of the expansion, we consider only the AC power input $Q = Q_0\cos(2\omega t)$ and the corresponding oscillating temperature rise and expansion but ignore the steady-state contribution (the steady-state terms can be obtained by letting $\omega = 0$ in the final solution). To solve the heat transfer equation, we represent the oscillating temperature in the PMMA as $\theta(x,y,t) = \theta_0(x,y)\exp(2i\omega t)$ and calculate $\theta_0(x,y)$ through the Fourier cosine transform (details appear in the Supporting Information, part 2) to find

$$\theta_0(x,y) = Q_0\sqrt{\frac{2}{\pi}}\int_0^{+\infty} A_0[\exp(y\sqrt{s^2+q_0^2}) + \exp(-y\sqrt{s^2+q_0^2} - 2h_0\sqrt{s^2+q_0^2})]\cdot\cos(sx)ds \qquad (2)$$

where

$$A_0 = (\kappa+1)\exp(h_0\sqrt{s^2+q_0^2})\sin\left(\frac{\pi r_0}{2}s\right) / \pi r_0 s\sqrt{2\pi(s^2+q_1^2)}k_1\left[(1-\kappa)\cosh(h_0\sqrt{s^2+q_0^2}) + (\kappa+1)\frac{k_0\sqrt{s^2+q_0^2}}{k_1\sqrt{s^2+q_1^2}}\sinh(h_0\sqrt{s^2+q_0^2})\right]$$

$$\kappa = 1 - \frac{k_2}{k_1}\frac{\frac{\sqrt{s^2+q_2^2}}{\sqrt{s^2+q_1^2}}}{1+\frac{k_2}{k_1}\frac{\sqrt{s^2+q_2^2}}{\sqrt{s^2+q_1^2}}}\exp(-2h_1\sqrt{s^2+q_1^2}),$$

$$q_0^2 = \frac{2i\omega}{\alpha_0},\quad q_1^2 = \frac{2i\omega}{\alpha_1},\quad \text{and}\quad q_2^2 = \frac{2i\omega}{\alpha_2}$$

As an approximation, the contribution of SiO_2 and Si to the thermal expansion can be neglected since their coefficients of thermal expansion (CTE) ($\sim 1\times10^{-6}$) are more than 10 times smaller than that of PMMA ($\sim 5\times10^{-5}$). (We note that, although the Si substrate is thick, the temperature rise is significant only near its surface and diminishes quickly. This behavior leads to an approximately spatially uniform contribution to the total expansion, as shown in Figure S6.) Neglecting expansion in SiO_2 and Si allows an analytical study of the SJEM signal by considering expansion in a layer of PMMA that is traction-free at its top surface ($y = -h_0$) and fully constrained at its base ($y = 0$). The full solution, which appears in the Supporting Information, part 2, indicates that at low frequencies, when the thermal diffusion length for the PMMA is much larger than the PMMA thickness (for purposes here, we define this length as $L_D = (\alpha_0/\omega)^{1/2} \gg h_0$), the temperature throughout the thickness of PMMA is approximately equal to its surface temperature, and the amplitude of the oscillating vertical displacement at the PMMA top

surface (*i.e.*, the detected thermal expansion in experiment) can be written simply as

$$|u_y(x, -h_0)| = \frac{1+\nu_0}{1-\nu_0}\beta_0 h_0 |\theta_0(x, -h_0)| \quad (3)$$

where ν_0 and β_0 are the Poisson's ratio and CTE of PMMA, respectively (see Figure S4 for comparisons of the simplified formula with the full solution at different frequencies). We also performed coupled thermo-mechanical FEA to verify the results of the analytical treatment (see Methods section).

On the basis of such models, the measured cross-sectional SJEM profiles can be fit using the power dissipation per unit length Q_0 as the only free parameter, with all other material constants taken from the literature[34−43] (see Supporting Information, Table S1). The results appear as red lines (analytical) and green dots (FEA) in Figure 3d,e. When $Q_0 \sim 3.9$ μW/μm for cross section A and ~1.7 μW/μm for cross section B, the computed results match the measured ones remarkably well. Repetitively fitting each measured cross section yields Q_0 as a function of position along the SWNT. Integration yields a total power of ~14.6 μW, which compares well to the measured total input power of ~18 μW. The fact that most of the power (~81%) is dissipated in the device channel is consistent with modest resistances at the electrical contacts.

A simple, complementary way to consider the results is to note that the temperature increase of the SWNT can be written as $\theta_{SWNT} = Q_0(1/g_{int} + 1/g_{sur})$, where g_{int} is the interfacial thermal conductance per unit length along the tube[6,31] (at the interfaces between SWNT and PMMA, SiO_2), and g_{sur} is the spreading thermal conductance from the surroundings of the SWNT to the ambient, including contributions from PMMA, SiO_2, and Si. The analytical expressions in eq 2 yield values for $g_{sur} = Q_0/|\theta_0(0,0)| \approx 0.75$ and 0.73 W/m/K for $r_0 = 0.5$ and 0.6 nm, respectively. Literature reports suggest that $g_{int} = 2\pi r_0 h$ ($g_{int} \approx 0.47$ W/m/K for $r_0 = 0.5$ nm and 0.57 W/m/K for $r_0 = 0.6$ nm), where $h = 1.5 \times 10^8$ W/m^2/K is the thermal coupling per unit area for typical metallic SWNTs.[31] With these parameters and radii of $r_0 = 0.5$ and 0.6 nm for the hotter and colder segments, respectively, we obtain temperature distributions that are consistent with measurement and modeling (Figure 3f). This profile accurately reflects the distinct heating from the two segments, except within a few hundred nanometers (the thermal transfer length[6,7]) near the metal contacts and the joint region between the hotter and colder segments, where the temperature is somewhat overestimated (see Figure S8d and Figure S9) due to inaccuracies that arise from application of the 2D analysis to regions with non-uniform heating.

The achievable levels of spatial and temperature resolution are important characteristics of the measurement. To examine the limits of the technique, and to further understand heat flow from the SWNT, we

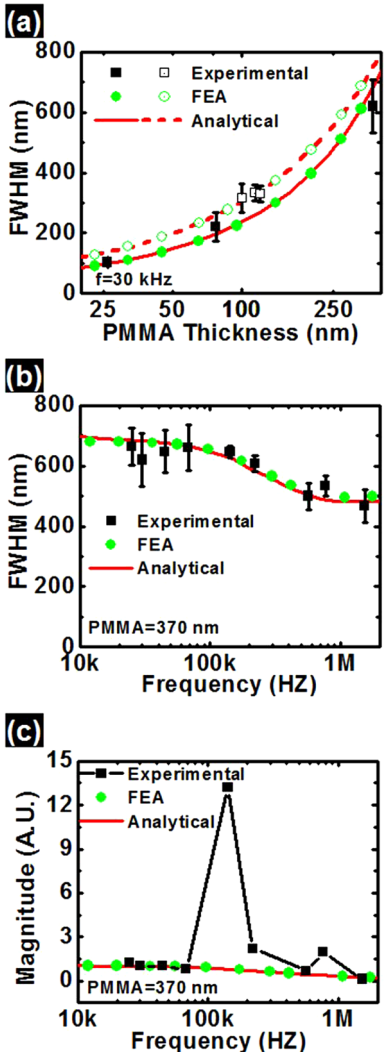

Figure 4. (a) Effects of PMMA and SiO_2 thicknesses on the resolution (represented by the full width at half-maximum, fwhm) in SJEM measurements: measurements, FEA, and analytical modeling of the widths (fwhm) for the expansion profiles across the SWNT, at f = 30 kHz. Data collected for PMMA of various thicknesses on two types of device substrates (hollow squares, hollow circles, and dashed lines correspond to SiO_2/Si (200 nm/500 μm); solid squares, solid circles, and solid lines correspond to SiO_2/Si (90 nm/300 μm)). The x-axis uses a log-scale. (b) Effects of frequency on the resolution of SJEM: measurements, FEA, and analytical modeling of the fwhm at different frequencies, for the case of PMMA and SiO_2 thicknesses of 370 and 90 nm, respectively. (c) Measurements, FEA, and analytical modeling of the expansion magnitude at different frequencies for the case of PMMA and SiO_2 thicknesses of 370 and 90 nm, respectively. Here, the thermo-mechanical simulation does not include the effects of tip-contact resonances that appear prominently around 150 kHz (see text and Supporting Information).

studied devices with different thicknesses of SiO_2 and PMMA. Figure 4a shows the characteristic widths (full width at half-maximum, fwhm) of the measured temperature signal along the sample surface and across individual SWNTs, similar to those in Figure 3d,e, on 90 nm (solid square) and 200 nm (hollow square) thick layers of SiO_2, imaged at f = 30 kHz. Also shown are

results of FEA (solid and hollow circles) and analytical modeling (solid and dashed lines). Throughout the range of PMMA thicknesses (25 to 370 nm), the fwhm values of profiles for the 90 nm SiO_2 case are smaller than those for 200 nm SiO_2. Likewise, the fwhm decreases almost linearly with thickness of the PMMA, corresponding to an increase in spatial resolution. (Results for PMMA thickness extending to 1.5 μm appear in Figure S7a.) In all cases, experiment agrees well with modeling. We note that the temperature signal is a convolution of the thermo-mechanical expansion, which is mostly in the vertical direction, and the temperature field near the CNT, which varies in both the vertical and lateral directions.

The temperature resolution, defined as the temperature rise in the SWNT that causes the smallest detectable expansion signal, can be represented as $\delta T = ((\delta h)/(|u_y(0,-h_0)|/Q_0)\ (1/g_{int} + 1/g_{sur})$, where δh is the noise equivalent height. This latter parameter originates from cantilever noise[25] and both mechanical and electrical noise in the AFM system. The thermo-mechanical expansion is almost entirely in the vertical direction, which simplifies analysis of the temperature resolution.[28] For typical experimental conditions ($f <$ 90 kHz, Asylum ACT 240 cantilever, bandwidth for the lock-in amplifier between 3.4 and 35 Hz), δh is between 0.7 and 1.6 pm. The temperature resolution δT also depends on the thermo-mechanical expansion of the PMMA (*i.e.*, $u_y(0,-h_0)/Q_0$). As the PMMA thickness increases, the total expansion signal increases for a given temperature rise, thereby providing an improved temperature resolution (see Figure S7b for the expansion signal scaling with PMMA thickness). Finally, the interfacial thermal resistance between the SWNT and surroundings further decreases δT. The temperature resolution for the SWNT shown in Figure 3 is estimated to be ~0.7 K.

The dependence of the spatial resolution on operating frequency is also important and can be understood in terms of the thermal diffusion length. Figure 4b shows the fwhm values of the cross sections from the measured signals, for a SWNT on SiO_2/Si (90 nm/300 μm) with PMMA (370 nm) at different frequencies, including both experiment and modeling results. At low frequencies, the width remains nearly constant since the thermal diffusion length L_D of PMMA is large compared to its thickness. As the frequency increases, the width decreases, consistent with a reduction in L_D. Further increases in frequency leads to another regime of frequency-independent behavior, as L_D becomes comparable to and less than the thickness of PMMA. The magnitudes of the expansion signals show frequency dependence as well as illustrated in Figure 4c (solid square). Here, the green solid circles and red solid line correspond to the FEA results and analytical simulations, respectively. The general trend is that the expansion magnitude decreases as the frequency

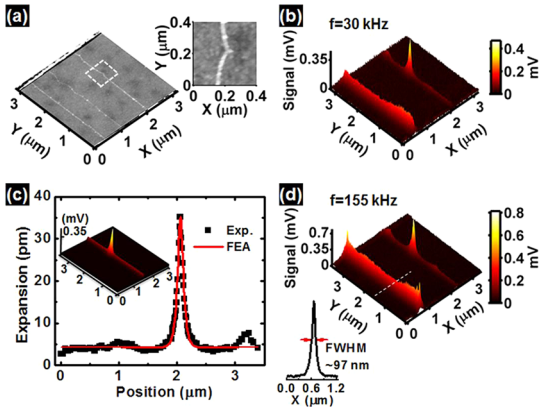

Figure 5. (a) Topographical AFM image of three SWNTs. The inset provides a magnified view of a "kink" in one of the SWNTs (highlighted by the white dashed box). (b) SJEM image of the same SWNTs. A strong peak appears at the position of the kink, consistent with significant heat generation at this location. (c) Expansion profile along the SWNT with the kink (solid square) and the results (red curve) based on a 3D FEA model that accounts for heat generation at the site of the defect. The power dissipation at the defect is calculated to be 2.9 μW, while the rest of the SWNT has an average power density 3.0 μW/μm. The inset shows the results of full 3D FEA simulations. (d) SJEM image collected at high frequency shows an enhancement in the signal. The overall image is similar to (a) except for the portion near the metal−SWNT contact where the local stiffness of the substrate and the step in topography may influence the tip-contact resonances. The lower left inset provides a cross-section profile along the dotted line in (c), showing a fwhm smaller than 100 nm.

increases, with the exception of several data points that show anomalously large signals at frequencies near 150 kHz (see Figure S10 for comparing images taken at f = 30 and 142 kHz). This behavior is related to resonant vibrations of the tip (see Supporting Information, part 6) and is not included in the thermo-mechanical simulation. The implication here is that quantitative SJEM measurements can be most easily made at low frequencies, where the AFM tip simply follows the thermal expansion profiles. Although high-frequency operation increases the spatial resolution, measurements in this regime can be difficult to analyze quantitatively due to complexities associated with tip−sample interactions.

As a demonstration of the versatility of the technique when implemented with PMMA thicknesses optimized according to the results described above, SJEM can be used to examine SWNTs that have defects. SWNT devices, even formed with pristine SWNT grown by chemical vapor deposition (CVD), often include defects[44] that can affect their electronic properties.[5] SJEM can image these defects to determine not only their spatial positions but also their effects on charge transport, *via* influence on local Joule heating. Figure 5a presents an AFM topographic image of a device with three SWNTs. One of the SWNTs has a prominent kink in the middle of the channel, as shown by the magnified image (inset in Figure 5a). This kink results from growth and can be considered as

a topographic defect. Figure 5b shows a SJEM image of this device, imaged using a 25 nm thick coating of PMMA at a frequency of 30 kHz and $V_g = 0$ V. Here, one SWNT exhibits nearly uniform expansion along its length; another SWNT shows almost no signal (due to high combined resistances in the contacts and this particular SWNT); the third exhibits a sharp peak corresponding to the site of the kink defect. Extraction of the expansion magnitude along this SWNT (black squares in Figure 5c) shows that the signal of the defect is about 8 times higher than the average level along the remainder of this SWNT, indicating substantial local heating.

Using a 3D FEA model that incorporates a point heating source (total power Q_{def}) and a uniformly distributed line heating source (power density Q_{ave}) to represent the defect and other parts of the SWNT, respectively (see Methods and Supporting Information, part 7), can match the experimental expansion profiles. Here, the interfacial thermal resistance g_{int} is adjusted to control the thermal diffusion along the SWNT (thermal transfer length $L_T \sim (kA(1/g_{int} + 1/g_{sur}))^{1/2}$, where k is the thermal conductivity and A is the cross-section area of the SWNT),[6,7,31] thereby the shape of the expansion profile. The power is selected to match the magnitude of the expansion. By using $L_T \sim 40$ nm, $Q_{def} \sim 2.9$ μW, and $Q_{ave} = 3.0$ μW/μm, we achieved good agreement between the simulation and experiment, as shown by the red curve in Figure 5c. The plot in the inset shows the full solution from FEA (here, the simulated height values has been changed to the equivalent electronic readout values for better comparison with Figure 5a). The simulated $L_H \sim 40$ nm is smaller than a previously reported value[6] (~200 nm) inferred from electrical breakdown of SWNTs on SiO_2/Si. This difference is likely due in part to the additional, conformal PMMA layer, which facilitates heat removal from the SWNT (increases g_{int}), and in part to a likely lower thermal conductivity in this SWNT near the defect location. We note that, although the power dissipated at the defect site only consists ~22% of the total input power, its temperature is estimated to be considerably higher (~13 times) than that of the other regions of the SWNT.

For these results, the thin coating of PMMA enables high spatial resolution; low-frequency operation facilitates extraction of the power density and temperature quantitatively. To further increase the resolution as well as the signal magnitude, high-frequency imaging can be used, as shown in Figure 5d, collected at a frequency of 155 kHz. Here, the signal is enhanced due to resonant effects, as described in Figure 4c. The shape of the expansion is identical to the case evaluated at low frequency, except for regions of the sample near the edges of the metal contacts where contact stiffness of the AFM tip changes due, at least in part, to the sharp topographical features. This creates artificial peaks that do not accurately reflect the temperature (*i.e.*, heat conduction through the metal contacts in these regions should reduce the temperatures locally).[6,7] The resolution of the image, as shown in the inset of Figure 5d (corresponding to cross sections marked by the dotted line), is better than 100 nm.

CONCLUSIONS

The results provided here use SJEM to examine, in a quantitative fashion, the physics of heat generation and dissipation in a variety of devices that incorporate individual, isolated SWNTs as the active materials. Physical properties such as the chirality, diameter, and point defects strongly affect the measured temperature distributions. Analytical and FEA models account for all aspects of the thermo-mechanical response and provide tools for inferring temperature distributions from measurements of thermal expansion. By comparison to other techniques (Raman, IR, or SThM), SJEM has advantages of straightforward operation, quantitative interpretation, and high spatial resolution and sensitivity. The results provide an experimental and theoretical framework for accurate, precise thermal distribution measurements by SJEM, and the specific observations in SWNT devices yield insights into basic operational characteristics and heat flow properties in these systems.

METHODS

Fabrication and Characterization of SWNT Devices. Fabrication of the devices begins with the growth of aligned SWNTs on stable temperature (ST) cut single-crystal quartz (Hoffman Materials), using electron beam evaporated iron (0.1−0.4 Å) as the catalyst and ethanol as the feeding gas during the chemical vapor deposition (CVD) process.[45,46] Transfer of the SWNTs to a layer of thermally grown SiO_2 on a doped silicon wafer (SQI, Inc.) is carried out with methods described elsewhere.[47] Photolithography (AZ 5214), electron beam evaporation (AJA), and lift-off define the source−drain contacts (Ti/Pd, 1 nm/40 nm). Oxygen plasma etching of SWNTs that lie outside of the active channel through a photolithographically defined pattern of resist yields devices with one or several SWNTs. Some of the devices with single, individual SWNTs used tubes directly grown by CVD on SiO_2/Si substrates with catalyst islands of ferritin (Sigma Aldrich) patterned by photolithography.[48] Scanning electron microscopy (SEM, Hitachi 4800) enables selection of those devices with a desired number of SWNTs. Use of a semiconductor parameter analyzer (Agilent 4156) reveals the electrical characteristics.

SJEM Imaging. PMMA (950 A4 or 950 A2; Micro Chem) spin-cast onto devices at different spinning speeds and durations yields films with desired thicknesses. PMMA diluted in methoxybenzene enables access to thicknesses smaller than 50 nm. Baking the devices at 110 °C for 5−10 min after coating removes the residual solvent. AFM (Asylum MFP 3D) measurements at step edges corresponding to locations of physical removal of the PMMA near the devices yield accurate values of the thicknesses. Wire bonding the device to a sample holder (Spectrum Semiconductor Materials) allows measurement

while providing electrical connections for applying electrical bias. All of the SJEM measurements are performed under ambient conditions, in air. Evaluating the force/displacement curve of the cantilever (Asylum Olympus AC240TS) before scanning defines the relationship between the deflection and detector signal. During SJEM imaging, a function generator (Agilent 33250A) provides a sinusoidal voltage to the source–drain and a reference to the lock-in amplifier (Stanford SR844). A source meter (Keithley 2612) controls the back-gate voltage. The deflection signal induced by thermal expansion feeds into the lock-in amplifier to capture the amplitude and phase of the signal at twice the frequency of the oscillating applied potential (Figure S1).

Finite Element Analysis (FEA). FEA simulations rely on commercial software (COMSOL) with combined modules of heat conduction (transient) and mechanical stress–strain analysis (quasi-static). For the 2D model, a SWNT placed at the interface between the PMMA and SiO_2, with power dissipation per unit length $Q = Q_0(1 + \cos(2\omega t))$, serves as the Joule heating source. The width of the simulated domain is 200 μm. The thickness of the Si is 100 μm (Figure S5). Performing the transient thermal transport calculation by setting the bottom surface of the structure to a constant temperature (300 K), enforcing temperatures to be continuous across interfaces, and treating all other boundary surfaces as thermal insulating (theoretical estimates suggest that the heat losses from radiation and convection are negligible; see Supporting Information, part 8) yields the time-dependent temperature distribution. Calculation of thermal expansion uses a fully constrained bottom surface, traction-free boundaries for all other surfaces and no-slip condition at all interfaces. Table S1 lists the parameters used in the simulation. To ensure steady-state behavior, the results (*i.e.*, the amplitude of the out-of-plane thermal expansion at the top surface) are extracted from the final cycle of a simulation that includes 30–50 cycles of time oscillation (higher frequencies used more cycles). At small thicknesses of the PMMA, the interfacial thermal resistance at the PMMA/SiO_2 boundary is no longer negligible.[49,50] Here, the temperature continuity assumption leads to results that underestimate the actual temperature rise in the PMMA and thereby the thermal expansion. As an example, the expansion is underestimated by ~12% for the case of PMMA (25 nm)/SiO_2 (90 nm) and ~6% for the case of PMMA (120 nm)/SiO_2 (200 nm) if the PMMA/SiO_2 interfacial thermal resistance[51] is $\sim 10^{-8}$ m^2 kW^{-1}. The effect on the fwhm of the profiles is smaller than 2% in both cases.

For the 3D model used to simulate the case of a SWNT with a point defect, the power output per unit length $Q(x) = [Q_{def}\delta(x - x_0) + Q_{ave}(x)](1 + \cos(2\omega t))$ is used. Here, $x_0 = 2.05$ μm is the position of the defect, Q_{def} and Q_{ave} is the power density of the defect and the rest of the SWNT, respectively. The overall dimensions of the simulation are 3.4 μm (length) × 3 μm (width), with PMMA (25 nm)/SiO_2 (90 nm) and Si ignored for simplicity. Frequency is set as 30 kHz. All boundary conditions are set to be the same as those in the 2D case (*i.e.*, fixed temperature and motion at the bottom surface; thermal insulation and free of motion for all other surfaces), except for the additional interfacial thermal resistance of 1×10^{-8} m^2 kW^{-1} at the PMMA/SiO_2 interface and $1/g_{int}$ for the interface between SWNT and surrounding materials (PMMA/SiO_2). Five time cycles of oscillation are simulated, and results are extracted from the final cycle.

Conflict of Interest: The authors declare no competing financial interest.

Acknowledgment. We thank W. Yang for helping with the sample preparation, S. Maclaren for technique support on the AFM, and B. Bhatia for helpful discussions. This material is based upon work supported by the Semiconductor Research Corporation (SRC), Nanotechnology Research Initiative (NRI), and the U. S. Department of Energy, Division of Materials Sciences under Award Nos. DE-FG02-07ER46453 and DE-FG02-07ER46471, through the Frederick Seitz Materials Research Laboratory at the University of Illinois at Urbana—Champaign.

Supporting Information Available: (1) Details of the SJEM setup, (2) details of the 2D analytical model for thermal transport and thermo-mechanical response, (3) properties of the materials used in the analytical model and FEA, (4) additional 2D FEA, (5) validation of the 2D models, (6) tip–sample interaction and the resonant enhancement effect, (7) simulation of thermo-mechanical response for point defects in SWNTs, (8) justification of the adiabatic thermal transport boundary condition used at the top surface of PMMA. This material is available free of charge *via* the Internet at http://pubs.acs.org.

REFERENCES AND NOTES

1. Avouris, P.; Chen, Z. H.; Perebeinos, V. Carbon-Based Electronics. *Nat. Nanotechnol.* **2007**, *2*, 605–615.
2. Franklin, A. D.; Luisier, M.; Han, S. J.; Tulevski, G.; Breslin, C. M.; Gignac, L.; Lundstrom, M. S.; Haensch, W. Sub-10 nm Carbon Nanotube Transistor. *Nano Lett.* **2012**, *12*, 758–762.
3. Naeemi, A.; Meindl, J. D. Carbon Nanotube Interconnects. *Annu. Rev. Mater. Res.* **2009**, *39*, 255–275.
4. Freitag, M.; Johnson, A. T.; Kalinin, S. V.; Bonnell, D. A. Role of Single Defects in Electronic Transport through Carbon Nanotube Field-Effect Transistors. *Phys. Rev. Lett.* **2002**, *89*, 216801.
5. Purewal, M. S.; Hong, B. H.; Ravi, A.; Chandra, B.; Hone, J.; Kim, P. Scaling of Resistance and Electron Mean Free Path of Single-Walled Carbon Nanotubes. *Phys. Rev. Lett.* **2007**, *98*, 186808.
6. Pop, E.; Mann, D. A.; Goodson, K. E.; Dai, H. J. Electrical and Thermal Transport in Metallic Single-Wall Carbon Nanotubes on Insulating Substrates. *J. Appl. Phys.* **2007**, *101*, 093710.
7. Xiong, F.; Liao, A.; Pop, E. Inducing Chalcogenide Phase Change with Ultra-Narrow Carbon Nanotube Heaters. *Appl. Phys. Lett.* **2009**, *95*, 243103.
8. Deshpande, V. V.; Hsieh, S.; Bushmaker, A. W.; Bockrath, M.; Cronin, S. B. Spatially Resolved Temperature Measurements of Electrically Heated Carbon Nanotubes. *Phys. Rev. Lett.* **2009**, *102*, 105501.
9. Li, Q. W.; Liu, C. H.; Wang, X. S.; Fan, S. S. Measuring the Thermal Conductivity of Individual Carbon Nanotubes by the Raman Shift Method. *Nanotechnology* **2009**, *20*, 145702.
10. Tsai, C. L.; Liao, A.; Pop, E.; Shim, M. Electrical Power Dissipation in Semiconducting Carbon Nanotubes on Single Crystal Quartz and Amorphous SiO_2. *Appl. Phys. Lett.* **2011**, *99*, 053120.
11. Estrada, D.; Pop, E. Imaging Dissipation and Hot Spots in Carbon Nanotube Network Transistors. *Appl. Phys. Lett.* **2011**, *98*, 073102.
12. Hu, X. J.; Panzer, M. A.; Goodson, K. E. Infrared Microscopy Thermal Characterization of Opposing Carbon Nanotube Arrays. *J. Heat Transfer* **2007**, *129*, 91–93.
13. Shi, L.; Plyasunov, S.; Bachtold, A.; McEuen, P. L.; Majumdar, A. Scanning Thermal Microscopy of Carbon Nanotubes Using Batch-Fabricated Probes. *Appl. Phys. Lett.* **2000**, *77*, 4295–4297.
14. Small, J. P.; Shi, L.; Kim, P. Mesoscopic Thermal and Thermoelectric Measurements of Individual Carbon Nanotubes. *Solid State Commun.* **2003**, *127*, 181–186.
15. Shi, L.; Zhou, J. H.; Kim, P.; Bachtold, A.; Majumdar, A.; McEuen, P. L. Thermal Probing of Energy Dissipation in Current-Carrying Carbon Nanotubes. *J. Appl. Phys.* **2009**, *105*, 104306.
16. Jo, I.; Hsu, I. K.; Lee, Y. J.; Sadeghi, M. M.; Kim, S.; Cronin, S.; Tutuc, E.; Banerjee, S. K.; Yao, Z.; Shi, L. Low-Frequency Acoustic Phonon Temperature Distribution in Electrically Biased Graphene. *Nano Lett.* **2011**, *11*, 85–90.
17. Yu, Y. J.; Han, M. Y.; Berciaud, S.; Georgescu, A. B.; Heinz, T. F.; Brus, L. E.; Kim, K. S.; Kim, P. High-Resolution Spatial Mapping of the Temperature Distribution of a Joule Self-Heated Graphene Nanoribbon. *Appl. Phys. Lett.* **2011**, *99*, 183105.
18. Shi, L.; Majumdar, A. Thermal Transport Mechanisms at Nanoscale Point Contacts. *J. Heat Transfer* **2002**, *124*, 329–337.
19. McConney, M. E.; Kulkarni, D. D.; Jiang, H.; Bunning, T. J.; Tsukruk, V. V. A New Twist on Scanning Thermal Microscopy. *Nano Lett.* **2012**, *12*, 1218–1223.

20. Menges, F.; Riel, H.; Stemmer, A.; Gotsmann, B. Quantitative Thermometry of Nanoscale Hot Spots. *Nano Lett.* **2012**, *12*, 596–601.
21. Shi, L.; Kwon, O.; Miner, A. C.; Majumdar, A. Design and Batch Fabrication of Probes for Sub-100 nm Scanning Thermal Microscopy. *J. Microelectromech. Syst.* **2001**, *10*, 370–378.
22. Kim, K.; Jeong, W. H.; Lee, W. C.; Reddy, P. Ultra-High Vacuum Scanning Thermal Microscopy for Nanometer Resolution Quantitative Thermometry. *ACS Nano* **2012**, *6*, 4248–4257.
23. Kim, K.; Chung, J.; Hwang, G.; Kwon, O.; Lee, J. S. Quantitative Measurement with Scanning Thermal Microscope by Preventing the Distortion Due to the Heat Transfer through the Air. *ACS Nano* **2011**, *5*, 8700–8709.
24. Park, K.; Cross, G. L. W.; Zhang, Z. M. M.; King, W. P. Experimental Investigation on the Heat Transfer between a Heated Microcantilever and a Substrate. *J. Heat Transfer* **2008**, *130*, 102401.
25. Majumdar, A.; Varesi, J. Nanoscale Temperature Distributions Measured by Scanning Joule Expansion Microscopy. *J Heat Transfer* **1998**, *120*, 297–305.
26. Varesi, J.; Majumdar, A. Scanning Joule Expansion Microscopy at Nanometer Scales. *Appl. Phys. Lett.* **1998**, *72*, 37–39.
27. Ho, X. N.; Ye, L. N.; Rotkin, S. V.; Xie, X.; Du, F.; Dunham, S.; Zaumseil, J.; Rogers, J. A. Theoretical and Experimental Studies of Schottky Diodes That Use Aligned Arrays of Single-Walled Carbon Nanotubes. *Nano. Res.* **2010**, *3*, 444–451.
28. Gurrum, S. P.; King, W. P.; Joshi, Y. K.; Ramakrishna, K. Size Effect on the Thermal Conductivity of Thin Metallic Films Investigated by Scanning Joule Expansion Microscopy. *J Heat Transfer* **2008**, *130*, 082403.
29. Bolte, J.; Niebisch, F.; Pelzl, J.; Stelmaszyk, P.; Wieck, A. D. Study of the Hot Spot of an In-Plane Gate Transistor by Scanning Joule Expansion Microscopy. *J. Appl. Phys.* **1998**, *84*, 6917–6922.
30. Grosse, K. L.; Bae, M. H.; Lian, F. F.; Pop, E.; King, W. P. Nanoscale Joule Heating, Peltier Cooling and Current Crowding at Graphene–Metal Contacts. *Nat. Nanotechnol.* **2011**, *6*, 287–290.
31. Liao, A.; Alizadegan, R.; Ong, Z. Y.; Dutta, S.; Xiong, F.; Hsia, K. J.; Pop, E. Thermal Dissipation and Variability in Electrical Breakdown of Carbon Nanotube Devices. *Phys. Rev. B* **2010**, *82*, 205406.
32. Jin, S. H.; Islam, A. E.; Kim, T. I.; Kim, J. H.; Alam, M. A.; Rogers, J. A. Sources of Hysteresis in Carbon Nanotube Field-Effect Transistors and Their Elimination *via* Methylsiloxane Encapsulants and Optimized Growth Procedures. *Adv. Funct. Mater.* **2012**, *22*, 2276–2284.
33. Joh, D. Y.; Herman, L. H.; Ju, S. Y.; Kinder, J.; Segal, M. A.; Johnson, J. N.; Chan, G. K. L.; Park, J. On-Chip Rayleigh Imaging and Spectroscopy of Carbon Nanotubes. *Nano Lett.* **2011**, *11*, 1–7.
34. Liu, W. J.; Etessam-Yazdani, K.; Hussin, R.; Asheghi, M. Modeling and Data for Thermal Conductivity of Ultrathin Single-Crystal Soi Layers at High Temperature. *IEEE Trans. Electron Devices* **2006**, *53*, 1868–1876.
35. Ju, Y. S.; Goodson, K. E. Process-Dependent Thermal Transport Properties of Silicon-Dioxide Films Deposited Using Low-Pressure Chemical Vapor Deposition. *J. Appl. Phys.* **1999**, *85*, 7130–7134.
36. Assael, M. J.; Botsios, S.; Gialou, K.; Metaxa, I. N. Thermal Conductivity of Polymethyl Methacrylate (PMMA) and Borosilicate Crown Glass Bk7. *Int. J. Thermophys.* **2005**, *26*, 1595–1605.
37. Tsutsumi, N.; Kiyotsukuri, T. Measurement of Thermal-Diffusivity for Polymer Film by Flash Radiometry. *Appl. Phys. Lett.* **1988**, *52*, 442–444.
38. Okada, Y.; Tokumaru, Y. Precise Determination of Lattice-Parameter and Thermal-Expansion Coefficient of Silicon between 300-K and 1500-K. *J. Appl. Phys.* **1984**, *56*, 314–320.
39. Blech, I.; Cohen, U. Effects of Humidity on Stress in Thin Silicon Dioxide Films. *J. Appl. Phys.* **1982**, *53*, 4202–4207.
40. Chou, S. Y.; Krauss, P. R. Imprint Lithography with Sub-10 nm Feature Size and High Throughput. *Microelectron. Eng.* **1997**, *35*, 237–240.
41. Wortman, J. J.; Evans, R. A. Youngs Modulus Shear Modulus and Poissons Ratio in Silicon and Germanium. *J. Appl. Phys.* **1965**, *36*, 153–156.
42. Kim, M. T. Influence of Substrates on the Elastic Reaction of Films for the Microindentation Tests. *Thin Solid Films* **1996**, *283*, 12–16.
43. Wu, W. L.; Vanzanten, J. H.; Orts, W. J. Film Thickness Dependent Thermal-Expansion in Ultrathin Poly(methyl methacrylate) Films on Silicon. *Macromolecules* **1995**, *28*, 771–774.
44. Fan, Y. W.; Goldsmith, B. R.; Collins, P. G. Identifying and Counting Point Defects in Carbon Nanotubes. *Nat. Mater.* **2005**, *4*, 906–911.
45. Xiao, J. L.; Dunham, S.; Liu, P.; Zhang, Y. W.; Kocabas, C.; Moh, L.; Huang, Y. G.; Hwang, K. C.; Lu, C.; Huang, W.; Rogers, J. A. Alignment Controlled Growth of Single-Walled Carbon Nanotubes on Quartz Substrates. *Nano Lett.* **2009**, *9*, 4311–4319.
46. Hong, S. W.; Banks, T.; Rogers, J. A. Improved Density in Aligned Arrays of Single-Walled Carbon Nanotubes by Sequential Chemical Vapor Deposition on Quartz. *Adv. Mater.* **2010**, *22*, 30–30.
47. Kang, S. J.; Kocabas, C.; Kim, H. S.; Cao, Q.; Meitl, M. A.; Khang, D. Y.; Rogers, J. A. Printed Multilayer Superstructures of Aligned Single-Walled Carbon Nanotubes for Electronic Applications. *Nano Lett.* **2007**, *7*, 3343–3348.
48. Kocabas, C.; Pimparkar, N.; Yesilyurt, O.; Kang, S. J.; Alam, M. A.; Rogers, J. A. Experimental and Theoretical Studies of Transport through Large Scale, Partially Aligned Arrays of Single-Walled Carbon Nanotubes in Thin Film Type Transistors. *Nano Lett.* **2007**, *7*, 1195–1202.
49. Cahill, D. G. Heat Transport in Dielectric Thin Films and at Solid–Solid Interfaces. *Microscale Therm. Eng.* **1997**, *1*, 85–109.
50. Lee, S. M.; Cahill, D. G. Heat Transport in Thin Dielectric Films. *J. Appl. Phys.* **1997**, *81*, 2590–2595.
51. Losego, M. D.; Moh, L.; Arpin, K. A.; Cahill, D. G.; Braun, P. V. Interfacial Thermal Conductance in Spun-Cast Polymer Films and Polymer Brushes. *Appl. Phys. Lett.* **2010**, *97*, 011908.

Supplementary Information

Quantitative Thermal Imaging of Single Walled Carbon Nanotube Devices by Scanning Joule Expansion Microscopy

Xu Xie, [†] *Kyle L. Grosse,* [‡] *Jizhou Song,* [⊥] *Chaofeng Lu,* [§] *Simon Dunham,* [†] *Frank Du,* [†] *Ahmad E. Islam,* [†] *Yuhang Li,* [#]*Yihui Zhang,* [#] *Eric Pop,*[||] *Yonggang Huang,* [#] *William P. King,*[‡,*] *and John A. Rogers*[†,‡,*]

[†]Department of Materials Science and Engineering and Frederick Seitz Materials Research Laboratory,

University of Illinois at Urbana-Champaign, Urbana, Illinois 61801, United States

[‡]Department of Mechanical Science and Engineering

University of Illinois at Urbana-Champaign, Urbana, Illinois 61801, United States

[⊥] Department of Mechanical and Aerospace Engineering,

University of Miami, Coral Gables, Florida 33146, United States

[§] Department of Civil Engineering and Soft Matter Research Center

Zhejiang University, Hangzhou 310058, China

[||]Department of Electrical and Computer Engineering and Micro and Nanotechnology Laboratory,

University of Illinois at Urbana-Champaign, Urbana, Illinois 61801, United States

[#]Department of Mechanical Engineering and Department of Civil and Environmental Engineering,

Northwestern University, Evanston, Illinois 60208, United States

*E-mail: jrogers@uiuc.edu, wpk@illinois.edu

Table of Contents:

1. Details of the SJEM setup

Figure S1 shows a detailed schematic diagram of the scanning Joule expansion microscopy (SJEM) setup. The AFM tip scans the sample surface in contact mode. A laser-photodiode system detects the cantilever deflection caused by intrinsic height variations as well as those due to thermomechanical expansion. A lock-in amplifier operating at the Joule heating frequency captures the expansion signal to form the thermal expansion image. A feedback loop with a cut-off frequency much smaller than the Joule heating frequency processes the topographical signal to form the image and it also controls the piezoelectric stage for scanning[1].

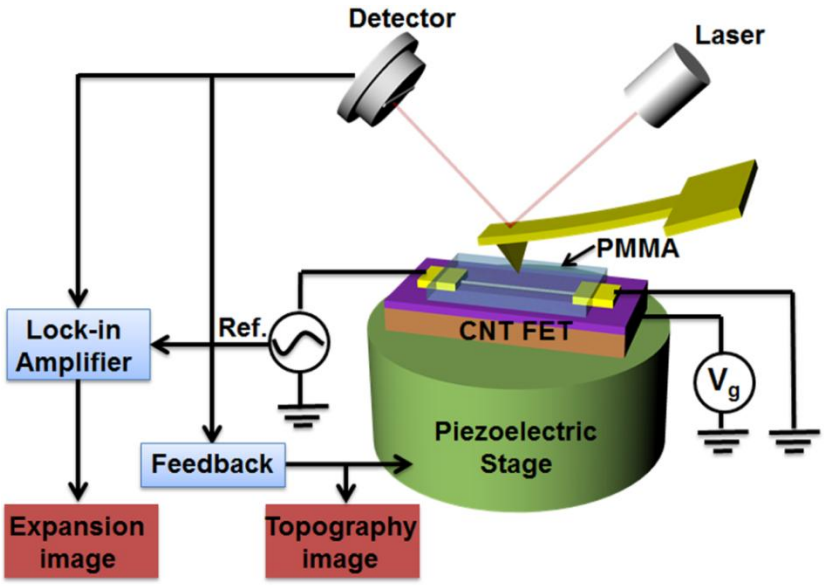

Figure S1. Detailed schematic diagram of the SJEM setup.

2. Details of the two dimensional (2D) analytical model for thermal transport and thermomechanical response

a) Temperature Distribution

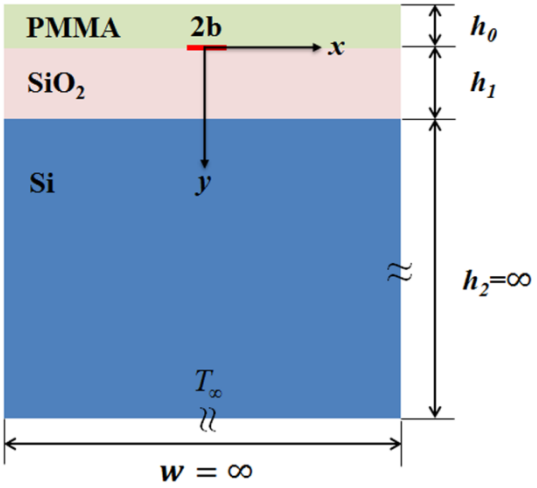

Figure S2. Schematic illustration of the domain for the 2D analytical model

The 2D heat transfer governing equation temperature is

$$\frac{\partial T}{\partial t}-\left(\frac{k}{c\rho}\right)\left(\frac{\partial^2 T}{\partial x^2}+\frac{\partial^2 T}{\partial y^2}\right)=0 \quad (1)$$

where k is thermal conductivity, ρ is density, c is specific heat capacity, and $\alpha = k/(c\rho)$ is thermal diffusivity. In the equations below, the subscripts 0, 1 and 2 denote PMMA, SiO_2 and Si, respectively. Setting $\theta = T - T_\infty$, where T_∞ is the ambient temperature, the above equation is equivalent to

$$\frac{\partial \theta}{\partial t}-(\frac{k}{c\rho})(\frac{\partial^2 \theta}{\partial x^2}+\frac{\partial^2 \theta}{\partial y^2})=0 \quad (2)$$

Due to symmetry ($\left.\frac{\partial \theta}{\partial x}\right|_{x=0}=0$), we only focus on the region with $x \geq 0$. The boundary conditions are

(1) $y=-h_0$ (top surface)

$$-k_0\left.\frac{\partial \theta}{\partial y}\right|_{y=-h_0}=0 \quad (3)$$

(2) $y=0$ ($PMMA/SiO_2$ interface)

$$\theta\Big|_{y=0^-} = \theta\Big|_{y=0^+},\ -k_0\frac{\partial\theta}{\partial y}\Big|_{y=0^-} = \begin{cases} P_0 & 0 \le x \le b \\ P_{c0} & b < x < +\infty \end{cases},\ -k_1\frac{\partial\theta}{\partial y}\Big|_{y=0^+} = \begin{cases} P_1 & 0 \le x \le b \\ P_{c1} & b < x < +\infty \end{cases} \quad (4)$$

where $b=\pi r_0/2$ (r_0 is the radius of the SWNT) is the half width of the heat source; P_0 and P_1 is the heat flux from the heat source at the interface, which satisfy $-P_0 + P_1 = \frac{Q}{2b}$, Q is the power dissipation per unit length along the SWNT; P_{c0} and P_{c1} is the heat flux at the interface where no heat source presents, which satisfy $-P_{c0} + P_{c1} = 0$ due to the continuity (note P_{c0} and P_{c1} are included to show the completeness of the boundary condition; they are not needed to obtain the temperature distribution).

(3) $y = h_1$ (SiO_2/Si interface)

$$\theta\Big|_{y=h_1^-} = \theta\Big|_{y=h_1^+} \text{ and } -k_1\frac{\partial\theta}{\partial y}\Big|_{y=h_1^-} = -k_2\frac{\partial\theta}{\partial y}\Big|_{y=h_1^+} \quad (5)$$

(4) $y = h_1 + h_2 \sim \infty$

$$\theta\Big|_{h_1+h_2} = 0 \quad (6)$$

For an applied voltage $V = V_{ds}\cos(\omega t)$ with the angular frequency $\omega = 2\pi f$, the Joule heating power density is $Q = Q_0(1+\cos(2\omega t))$, which has both DC (*i.e.* Q_0) and AC (*i.e.* $Q_0\cos(2\omega t)$) components. In the following, we will obtain the solution for the AC component, which corresponds to the measurements of SJEM. Assuming the alternating temperature rise is $\theta(x,y,t) = \tilde{\theta}(x,y)\exp(2i\omega t)$, we have

$$\frac{\partial^2\tilde{\theta}}{\partial x^2} + \frac{\partial^2\tilde{\theta}}{\partial y^2} - q^2\tilde{\theta} = 0 \quad (7)$$

where $q^2 = \frac{2\omega i}{\alpha}$.

Eq. (7) can be solved *via* the Fourier cosine transform

$$\begin{aligned} \bar{\tilde{\theta}}(s,y) &= \sqrt{\frac{2}{\pi}}\int_0^{+\infty}\tilde{\theta}(x,y)\cdot\cos(sx)dx \\ \tilde{\theta}(x,y) &= \sqrt{\frac{2}{\pi}}\int_0^{+\infty}\bar{\tilde{\theta}}(s,y)\cdot\cos(sx)ds \end{aligned}, \quad (8)$$

we have

$$-(s^2+q^2)\bar{\bar{\theta}}+\frac{\partial^2\bar{\bar{\theta}}}{\partial y^2}=0 \tag{9}$$

Solving the above equation gives

$$\begin{aligned}\bar{\bar{\theta}} &= A\exp(y\sqrt{s^2+q^2})+B\exp(-y\sqrt{s^2+q^2})\\ \frac{d\bar{\bar{\theta}}}{dy} &= A\sqrt{s^2+q^2}\exp(y\sqrt{s^2+q^2})-B\sqrt{s^2+q^2}\exp(-y\sqrt{s^2+q^2})\end{aligned} \tag{10}$$

where A and B are to be obtained from the boundary conditions. The temperature is then obtained by

$$\tilde{\theta}(x,y)=\sqrt{\frac{2}{\pi}}\int_0^{+\infty}\left[A\exp(y\sqrt{s^2+q^2})+B\exp(-y\sqrt{s^2+q^2})\right]\cdot\cos(sx)ds \tag{11}$$

Therefore, the temperature in Fourier space at each layer is obtained as:

PMMA layer: $\bar{\bar{\theta}}_0(s,y)=A_0\exp(y\sqrt{s^2+q_0^2})+B_0\exp(-y\sqrt{s^2+q_0^2})$

SiO_2 layer: $\bar{\bar{\theta}}_1(s,y)=A_1\exp(y\sqrt{s^2+q_1^2})+B_1\exp(-y\sqrt{s^2+q_1^2})$

Si layer: $\bar{\bar{\theta}}_2(s,y)=A_2\exp(y\sqrt{s^2+q_2^2})+B_2\exp(-y\sqrt{s^2+q_2^2})$

With boundary conditions (3)-(6) in Fourier space, we can obtain the temperature at each layer. For example, A_0 and B_0 are given by

$$A_0=\frac{Q_0(\kappa+1)\exp(h_0\sqrt{s^2+q_0^2})\sin(\frac{\pi r_0}{2}s)}{\pi r_0 s\sqrt{2\pi(s^2+q_1^2)}k_1\left[(1-\kappa)\cosh\left(h_0\sqrt{s^2+q_0^2}\right)+(\kappa+1)\frac{k_0\sqrt{s^2+q_0^2}}{k_1\sqrt{s^2+q_1^2}}\sinh\left(h_0\sqrt{s^2+q_0^2}\right)\right]} \tag{12}$$

$$B_0=A_0\exp(-2h_0\sqrt{s^2+q_0^2})$$

where $\kappa=\dfrac{1-\dfrac{k_2}{k_1}\dfrac{\sqrt{s^2+q_2^2}}{\sqrt{s^2+q_1^2}}}{1+\dfrac{k_2}{k_1}\dfrac{\sqrt{s^2+q_2^2}}{\sqrt{s^2+q_1^2}}}\exp(-2h_1\sqrt{s^2+q_1^2})$

The temperature in PMMA layer is then obtained as

$$\tilde{\theta}_0(x,y)=\sqrt{\frac{2}{\pi}}\int_0^{+\infty}A_0\left[\exp(y\sqrt{s^2+q_0^2})+\exp(-y\sqrt{s^2+q_0^2}-2h_0\sqrt{s^2+q_0^2})\right]\cdot\cos(sx)ds \tag{13}$$

b) Thermal Expansion Based on the temperature distribution

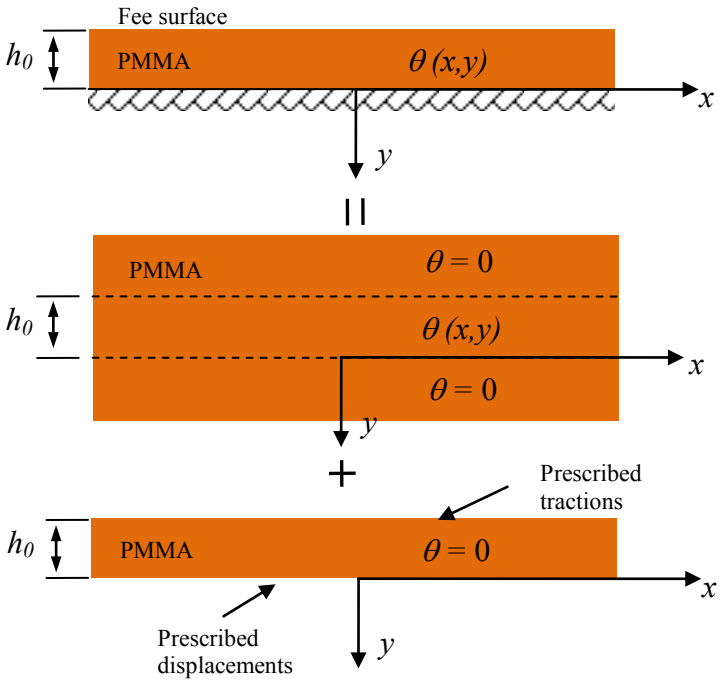

Figure S3. Schematic illustration of the thermo-mechanical model

Only the PMMA layer is considered in calculations of the thermal expansion. Its top surface is traction-free and the bottom surface is fully constrained. The problem is solved by superposing the following two solutions:

(1) Infinite plane with $\tilde{\theta}_0(x,y)$, and

(2) Finite plane without $\tilde{\theta}_0(x,y)$ but with its upper boundary tractions prescribed as the negative of σ_{yy} and σ_{xy} along $y=-h_0$, and the lower boundary displacements prescribed as the negative u and v calculated along $y=0$.

For problem (1), the potential of thermal displacement is given by

$$\psi(x,y)=\frac{1}{2\pi}\frac{1+\nu_0}{1-\nu_0}\beta_0\int_{\xi=-\infty}^{\infty}\int_{\eta=-h_0}^{0}\tilde{\theta}_0(\xi,\eta)\ln\sqrt{(x-\xi)^2+(y-\eta)^2}\,d\xi d\eta \qquad (14)$$

where ν_0 and β_0 are the Poisson ratio and coefficient of thermal expansion (CTE) of PMMA.

The displacements can be obtained

$$u_x = \frac{\partial \psi(x,y)}{\partial x} = \frac{1}{2\pi}\frac{1+\nu_0}{1-\nu_0}\beta_0 \int_{\xi=-\infty}^{\infty}\int_{\eta=-h_0}^{0} \tilde{\theta}_0(\xi,\eta)\frac{x-\xi}{(x-\xi)^2+(y-\eta)^2}\,d\xi d\eta$$
$$u_y = \frac{\partial \psi(x,y)}{\partial y} = \frac{1}{2\pi}\frac{1+\nu_0}{1-\nu_0}\beta_0 \int_{\xi=-\infty}^{\infty}\int_{\eta=-h_0}^{0} \tilde{\theta}_0(\xi,\eta)\frac{y-\eta}{(x-\xi)^2+(y-\eta)^2}\,d\xi d\eta \quad (15)$$

The stresses are given by

$$\sigma_x = -2G_0\frac{\partial^2\psi}{\partial y^2} = -\frac{1}{2\pi}\frac{E_0}{1-\nu_0}\beta_0 \int_{\xi=-\infty}^{\infty}\int_{\eta=-h_0}^{0} \tilde{\theta}_0(\xi,\eta)\frac{(x-\xi)^2-(y-\eta)^2}{\left[(x-\xi)^2+(y-\eta)^2\right]^2}\,d\xi d\eta$$
$$\sigma_y = -2G_0\frac{\partial^2\psi}{\partial x^2} = -\frac{1}{2\pi}\frac{E_0}{1-\nu_0}\beta_0 \int_{\xi=-\infty}^{\infty}\int_{\eta=-h_0}^{0} \tilde{\theta}_0(\xi,\eta)\frac{(y-\eta)^2-(x-\xi)^2}{\left[(x-\xi)^2+(y-\eta)^2\right]^2}\,d\xi d\eta \quad (16)$$
$$\sigma_{xy} = 2G_0\frac{\partial^2\psi}{\partial x\partial y} = -\frac{1}{2\pi}\frac{E_0}{1-\nu_0}\beta_0 \int_{\xi=-\infty}^{\infty}\int_{\eta=-h_0}^{0} \tilde{\theta}_0(\xi,\eta)\frac{2(x-\xi)(y-\eta)}{\left[(x-\xi)^2+(y-\eta)^2\right]^2}\,d\xi d\eta$$

where $G_0 = \frac{E_0}{2(1+\nu_0)}$ is the shear modulus of PMMA and E_0 is the Young's modulus of PMMA. The tractions at $y=-h_0$ are

$$\sigma_y^{h_0} = -\frac{1}{2\pi}\frac{E_0}{1-\nu_0}\beta_0 \int_{\xi=-\infty}^{\infty}\int_{\eta=-h_0}^{0} \tilde{\theta}_0(\xi,\eta)\frac{(h_0+\eta)^2-(x-\xi)^2}{\left[(x-\xi)^2+(h_0+\eta)^2\right]^2}\,d\xi d\eta$$
$$\sigma_{xy}^{h_0} = -\frac{1}{2\pi}\frac{E_0}{1-\nu_0}\beta_0 \int_{\xi=-\infty}^{\infty}\int_{\eta=-h_0}^{0} \tilde{\theta}_0(\xi,\eta)\frac{-2(x-\xi)(h_0+\eta)}{\left[(x-\xi)^2+(h_0+\eta)^2\right]^2}\,d\xi d\eta \quad (17)$$

The displacement at $y=0$ are

$$u_x^0 = \frac{1}{2\pi}\frac{1+\nu_0}{1-\nu_0}\beta_0 \int_{\xi=-\infty}^{\infty}\int_{\eta=-h_0}^{0} \tilde{\theta}_0(\xi,\eta)\frac{x-\xi}{(x-\xi)^2+\eta^2}\,d\xi d\eta$$
$$u_y^0 = \frac{1}{2\pi}\frac{1+\nu_0}{1-\nu_0}\beta_0 \int_{\xi=-\infty}^{\infty}\int_{\eta=-h_0}^{0} \tilde{\theta}_0(\xi,\eta)\frac{-\eta}{(x-\xi)^2+\eta^2}\,d\xi d\eta \quad (18)$$

For problem (2),

Consider the Airy stress function

$$\phi(x,y)=\frac{2}{\pi}\int_0^\infty \bar{\phi}(\xi,y)\cos(\xi x)\,d\xi \tag{19}$$

Substituting the above equations in the biharmonic equation and solving for ϕ, one can obtain

$$\phi(x,y)=\frac{2}{\pi}\int_0^\infty \left[\left(A_1+yA_2\right)e^{-\xi y}+\left(A_3+yA_4\right)e^{\xi y}\right]\cos(\xi x)\,d\xi \tag{20}$$

The stress components are given by

$$\sigma_{xx}=\frac{\partial\phi}{\partial y^2},\sigma_{yy}=\frac{\partial\phi}{\partial x^2},\sigma_{xy}=-\frac{\partial^2\phi}{\partial x\partial y} \tag{21}$$

Combining with the constitutive relation

$$\begin{aligned} e_x &= \frac{1}{E'}\left(\sigma_x-\nu'\sigma_y\right)\\ e_y &= \frac{1}{E'}\left(\sigma_y-\nu'\sigma_x\right)\\ e_{xy} &= \frac{1}{2G}\sigma_{xy} \end{aligned} \tag{22}$$

where $E'=\frac{E_0}{1-\nu_0^{\,2}},\nu'=\frac{\nu_0}{1-\nu_0}$, we can obtain the displacements

$$\begin{aligned} u_x(x,y) &= \frac{2}{\pi}\int_0^\infty \frac{1+\nu_0}{E_0}\left[\xi e^{-\xi y}A_1+\left(-2+2\nu+\xi y\right)e^{-\xi y}A_2+\xi e^{\xi y}A_3+\left(2-2\nu+\xi y\right)e^{\xi y}A_4\right]\sin(\xi x)\,d\xi\\ u_y(x,y) &= \frac{2}{\pi}\int_0^\infty \frac{1+\nu_0}{E_0}\left[\xi e^{-\xi y}A_1+\left(\xi y+1-2\nu\right)e^{-\xi y}A_2-\xi e^{\xi y}A_3-\left(\xi y-1+2\nu\right)e^{\xi y}A_4\right]\cos(\xi x)\,d\xi \end{aligned} \tag{23}$$

where A_1,A_2,A_3 and A_4 can be obtained from

$$\begin{bmatrix} -\xi^2e^{\xi h_0} & \xi^2h_0e^{\xi h_0} & -\xi^2e^{-\xi h_0} & \xi^2h_0e^{-\xi h_0}\\ -\xi^2e^{\xi h_0} & \left(\xi+\xi^2h_0\right)e^{\xi h_0} & \xi^2e^{-\xi h_0} & \left(\xi-\xi^2h_0\right)e^{-\xi h_0}\\ \xi & -2+2\nu & \xi & 2-2\nu\\ \xi & 1-2\nu & -\xi & 1-2\nu \end{bmatrix}\begin{Bmatrix} A_1\\A_2\\A_3\\A_4\end{Bmatrix}=-\begin{Bmatrix} \int_{x=0}^{\infty}\sigma_y^{h_0}\cos(\xi x)\,dx\\ \int_{x=0}^{\infty}\sigma_{xy}^{h_0}\sin(\xi x)\,dx\\ \int_{x=0}^{\infty}\frac{E_0}{1+\nu_0}u_x^0\sin(\xi x)\,dx\\ \int_{x=0}^{\infty}\frac{E_0}{1+\nu_0}u_y^0\cos(\xi x)\,dx \end{Bmatrix} \tag{24}$$

The superposition of problem (1) and problem (2) gives the out-of-plane displacement at $y=-h_0$ as

$$u_y\left(x,y=-h_0\right)=-\frac{1}{2\pi}\frac{1+\nu_0}{1-\nu_0}\beta_0\int_{\xi=-\infty}^{\infty}\int_{\eta=-h_0}^{0}\tilde{\theta}_0\left(\xi,\eta\right)\frac{h_0+\eta}{\left(x-\xi\right)^2+\left(h_0+\eta\right)^2}d\xi d\eta$$
$$\frac{2}{\pi}\int_0^{\infty}\frac{1+\nu_0}{E_0}\left[\xi e^{\xi h_0}A_1+\left(-\xi h_0+1-2\nu\right)e^{\xi h_0}A_2-\xi e^{-\xi h_0}A_3-\left(-\xi h_0-1+2\nu\right)e^{-\xi h_0}A_4\right]\cos\left(\xi x\right)d\xi \quad (25)$$

and its amplitude, which is the value measured by SJEM is $\left|u_y\left(x,y=-h_0\right)\right|$.

c) Thermal Expansion at Low Frequencies

The model in Section 2(b) above is accurate and does not involve any assumptions. At low frequencies, when the thermal diffusion length for PMMA is much larger than the PMMA thickness, the temperature throughout the thickness of PMMA is approximately equal to its surface temperature. Under the assumptions of (1) plane strain in *z* direction because the length of SWNT is much larger than its radius and (2) plane stress in *y* direction because the film is thin and the temperature is thickness independent, the amplitude of the oscillating vertical displacement of the PMMA top surface can be obtained as:

$$\left|u_y\left(x,-h_0\right)\right|=\frac{1+\nu_0}{1-\nu_0}\beta_0 h_0\left|\theta_0\left(x,-h_0\right)\right| \quad (26)$$

where ν_0 and β_0 are the Poisson's ratio and coefficient of thermal expansion (CTE) of the PMMA, respectively. Figure S4 clearly shows that the simple formula is valid for low frequencies (*e.g.*, smaller than 100 kHz, simulated for the case of PMMA thickness 120 nm and SiO_2 thickness 200 nm at Q_0 = 1 μW/μm heating along the SWNT).

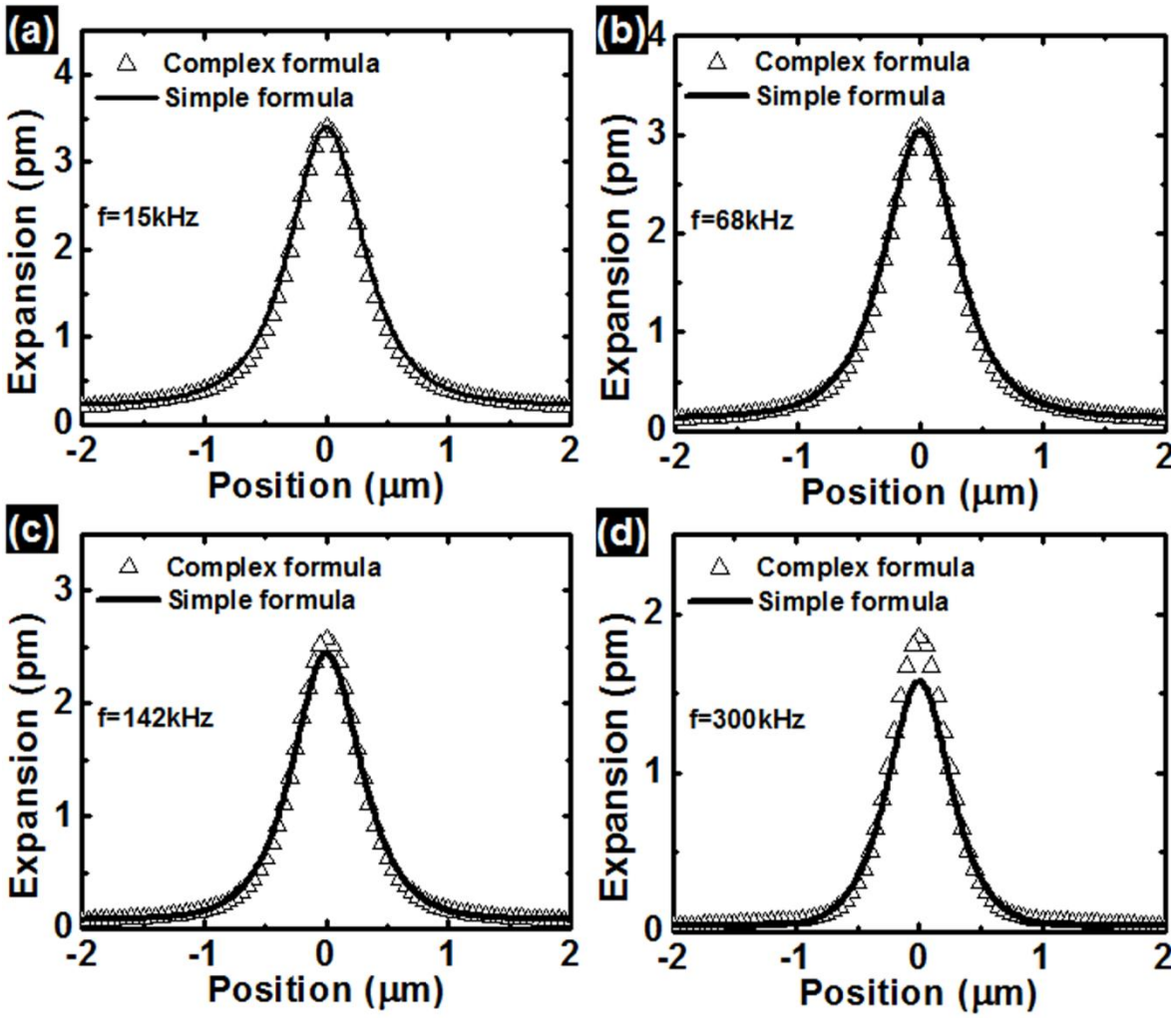

Figure S4. Comparison between the complex formula and the simplified one for (a) f = 15 kHz, (b), 68 kHz, (c) 142 kHz, (d) 300 kHz. Values are simulated for Q_0 = 1 μW/μm with PMMA thickness 120 nm and SiO_2 thickness 200 nm. The simplified formula serves as a good approximation when the frequency is low, *e.g.* <100 kHz for the physical conditions selected here.

3. Properties of the materials used in the analytical model and finite element analysis (FEA)

Table S1. Thermal and Mechanical parameters used in analytical and FE models

Materials	Thermal Conductivity ($Wm^{-1}K^{-1}$)	Thermal Diffusivity 10^{-6} (m^2s^{-1})	Coefficient of Thermal Expansion 10^{-6} (K^{-1})	Young's Modulus 10^9 (Pa)	Poisson Ratio
Si	120 (ref 2)	73	2.6 (ref 3)	165 (ref 4)	0.28 (ref 5)
SiO_2	1.3 (ref 6)	0.84 (ref 6)	0.50 (ref 7)	64 (ref 4)	0.17 (ref 8)
PMMA	0.19 (ref 9)	0.11 (ref 10)	50 (ref 11)	3.0 (ref 12)	0.35 (ref 13)

Note: Si is Boron doped, with resistivity ~0.005 $\Omega \cdot cm$.

4. Additional 2D FEA

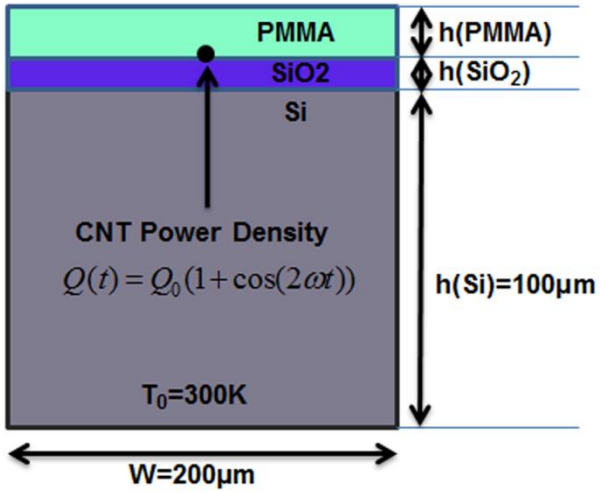

Figure S5. Structure used in the 2D FEA.

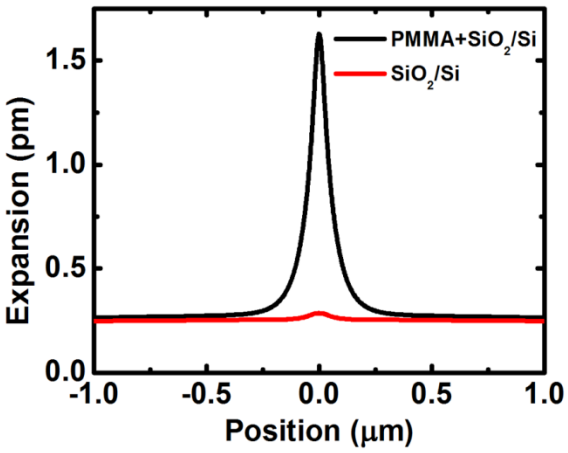

Figure S6. FEA simulation shows the total thermal expansion (black curve, extracted from the top surface of PMMA) and the thermal expansion of SiO_2/Si substrate (red curve). The contribution from SiO_2 is negligible due to very small CTE (~0.5x10^{-6} K^{-1}). Although the Si (CTE ~ 2.6 x10^{-6} K^{-1}) substrate is thick, its temperature rise is insignificant and broadly distributed. Therefore, together, the SiO_2/Si substrate only contributes a nearly flat background to the thermal expansion. The simulation is based on 25 nm PMMA and 90 nm SiO_2, at f = 30 kHz.

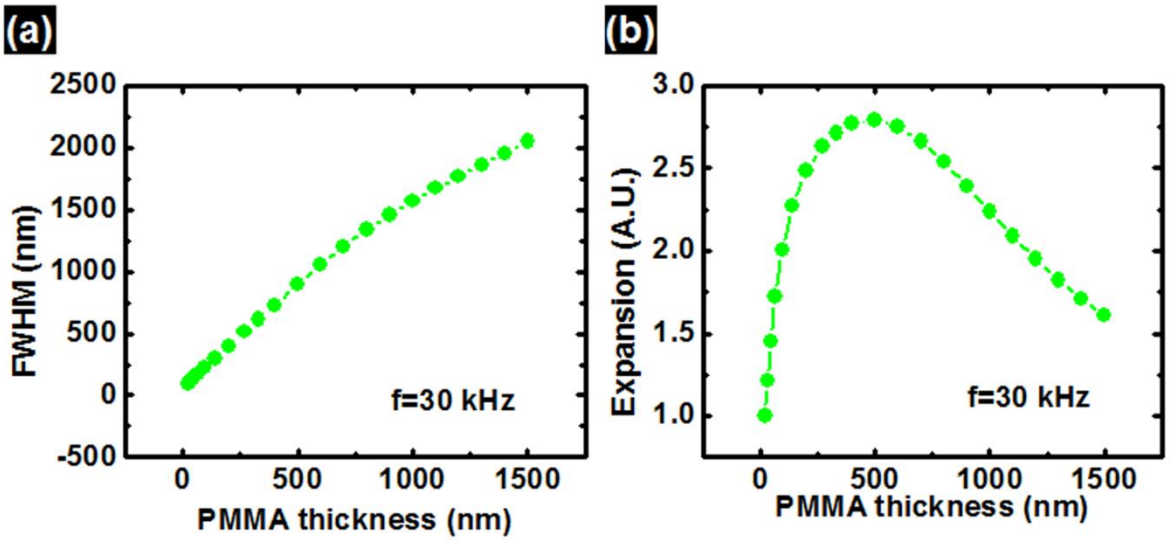

Figure S7. (a) Full width of half maximum (FWHM) for the expansion profiles across the SWNT with PMMA coating ranging from 25 nm to 1500 nm (Values are simulated at f = 30 kHz and SiO_2 thickness = 90 nm). (b) Expansion magnitude for SWNT with constant temperature (Values are simulated under the same conditions as (a)). The signal increases almost linearly with PMMA thickness when the

thickness is small (*e.g.* <100 nm), then reaches a maximum point (at ~500 nm here) and subsequently decreases, as the thermal diffusion length at this frequency becomes larger than the PMMA thickness.

5. Validation of the 2D models

A 3D FEA model was also built to justify the effectiveness of the 2D models. Figure S8a shows the structure used for the simulation. The width is 3 μm and the length of the left and right edges (where no SWNTs are present) are set to be at 2 μm. A SWNT placed at the interface between PMMA (120 nm) and SiO_2 (200 nm) has a diameter of 2 nm and power density of $Q_0 = 1\,\mu\text{W}/\mu\text{m}$. Ignoring the metal electrodes and the silicon substrate simplifies the calculation. Regarding thermal transport, the bottom surface of the structure and the two ends of the SWNT are set to a temperature of 300 K. All other boundary surfaces are thermal insulating and all interfaces are continuous. For calculations of the thermal expansion, the bottom surface is set to be fixed, all other boundary surfaces are free of motion and all the interfaces are characterized by no-slip behavior. Figure S8b shows the typical simulated result, where color represents the temperature and the exaggerated deformation indicates corresponding thermal expansion. Figure S8c shows how the cross-section of thermal expansion (across the center of the SWNT, along Y direction) changes with the length of the SWNT, together with a comparison to results from 2D models. The inset provides a plot of the maximum expansion (*i.e.* expansion value at Y = 0 μm in the cross-section) and its dependence on the lengths of the SWNTs. As the length increases, the magnitude of the cross-section also increases, finally approaching a constant value when L_{SWNT} is larger than about 1 μm (this value for 3D is smaller than that for 2D, because the 3D model here does not include the thick Si substrate, in which case the overall temperature and expansion are underestimated). The results indicate that the power will be overestimated if the 2D model is used for short channel devices (*e.g.* L < 1 μm) due to the effect of the contacts. Figure S8d provides a comparison between the temperature of the SWNT (red curve, here the SWNT is 2 μm) and the maximum thermal expansion on the PMMA surface (black curve), along the length of the SWNT (x direction). The shape of the thermal expansion curve matches the shape of the temperature curve. This

indicates that the 2D models are valid for calculating the temperature distribution along the SWNT (by fitting the cross section of the expansion at each point), with the exception of the regions near the contacts, where the expansion does not accurately reflect the temperature of the SWNT.

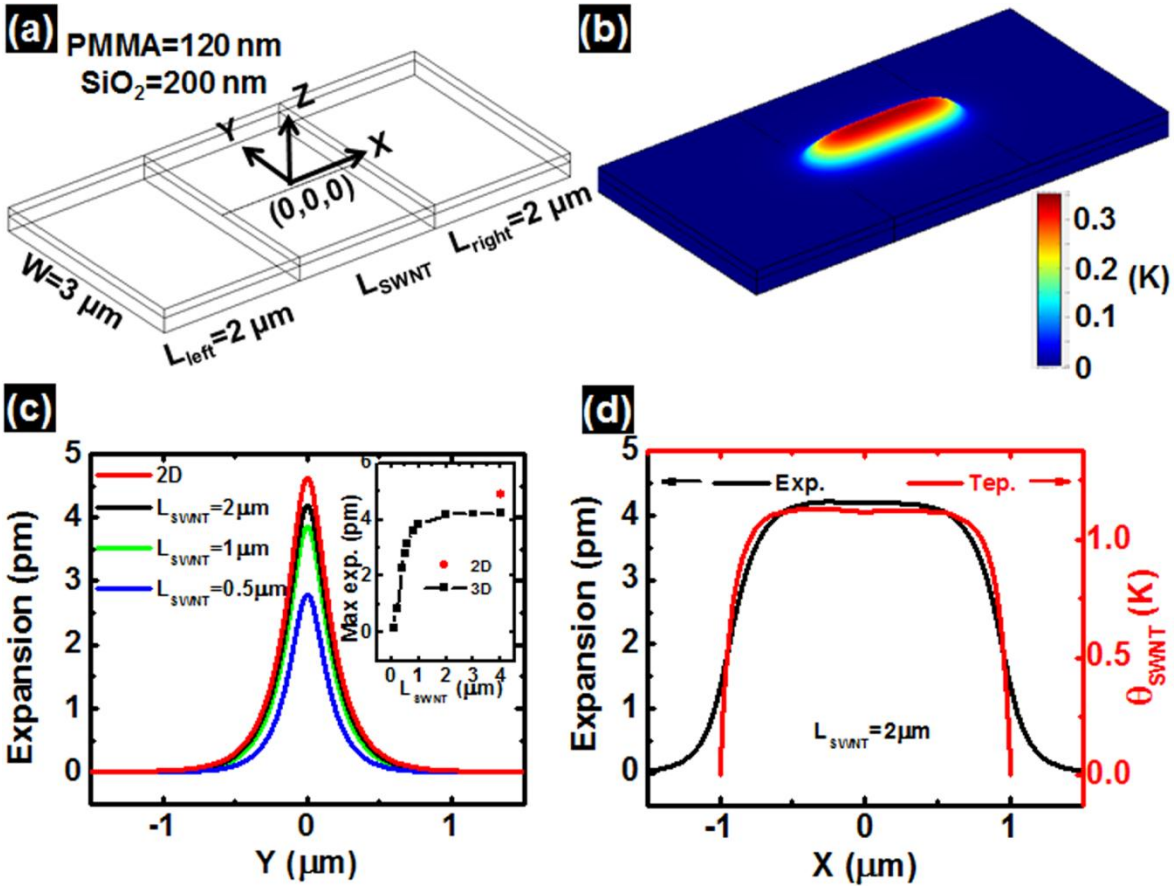

Figure S8. (a) Structure used for the 3D FEA simulation. (b) The result of a 3D simulation, where the color indicates the temperature and the deformation shows the corresponding thermal expansion. (c) Cross-sections of the thermal expansion (across the center of the SWNT, along Y direction) for SWNTs with different lengths, and the comparison with that from the 2D model. The inset shows how the maximum expansion (*i.e.* the point at Y = 0 μm in the cross-section) scales with the lengths of SWNTs. (d) The maximum expansion (black curve) along the length of the SWNT (X direction), and the temperature of the SWNT (red curve). Here the length of the SWNT is fixed as 2 μm.

Moreover, as a particular consideration, the SWNT shown in Figure 3 has a joint where two segments of distinct temperature merge. The 2D analysis near this location has some inaccuracies due to non-

uniformities in the temperature. To evaluate these errors, we note that the thermal transport characteristics at the joint region and the contact regions are essentially the same, *i.e.* both regions show temperature changes from one constant value to another constant value, and the transition distance is characterized by thermal transfer length L_T . Therefore, the analysis associated with Figure S8d not only reflects the errors caused by 2D analysis for the contact region, but the joint region as well.

To further understand the approximation, we solved the thermal transport equation along this SWNT,

$$kA\frac{\partial^2\theta(x,t)}{\partial x^2}+Q_0\cos(2\omega t)-(1/(\frac{1}{g_{\text{int}}}+\frac{1}{g_{sur}}))\theta(x,t)=\rho CA\frac{\partial\theta(x,t)}{\partial t} \qquad (27)$$

Here the SWNT is considered as of two segments, with input power density of Q_0=3.9 μW/μm, length~1.7 μm, diameter~1 nm for one segment and Q_0 = 1.7 μW/μm, length~4.1 μm, diameter~1.2 nm for the other one. The power and length are chosen to match the power density distribution and the total length of the SWNT; all boundary conditions and other physical parameters are the same with the 2D simulation described in the main text. In detail, the joint of the two segments are considered to have continuous heat flux and temperature change; Contacts of the SWNT are kept at room temperature. Thermal conductivity of SWNT k is 3000 W/m/K; $g_{\text{int}}=2\pi r_0 h$ ($h=1.5\times10^8\ \text{W/m}^2\text{/K}$) and g_{sur} □ $0.74W/m/K$ are the same with the 2D model. This 1D analytical treatment has been widely used for understanding the thermal transport along SWNTs.[14-17] As shown in figure S9, the resulting profile from the modeling matches fairly well with the one obtained from 2D analysis of the SJEM results (*i.e.* Figure 3f). As expected, per the discussion above, some similar inaccuracies exist at the contact and joint regions.

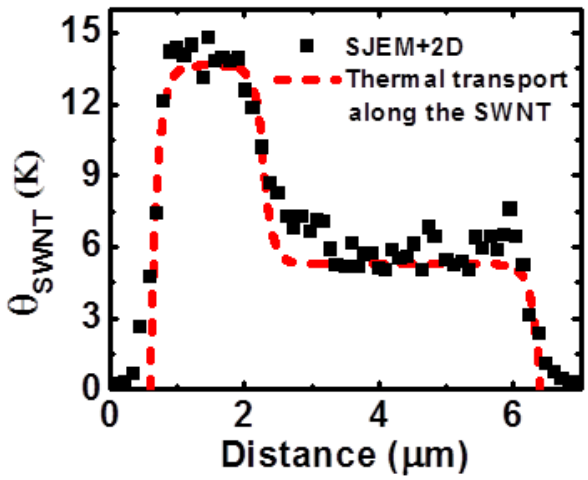

Figure S9. Comparison between the temperature profile (red dashed line) from solving the thermal transport equation along the SWNT and the one from 2D analysis (black solid square) of the SJEM results. Note most parts of the two profiles matches well except for those at the joint region and the contact regions, where similar differences exist.

6. Tip-sample interaction and the resonant enhancement effect

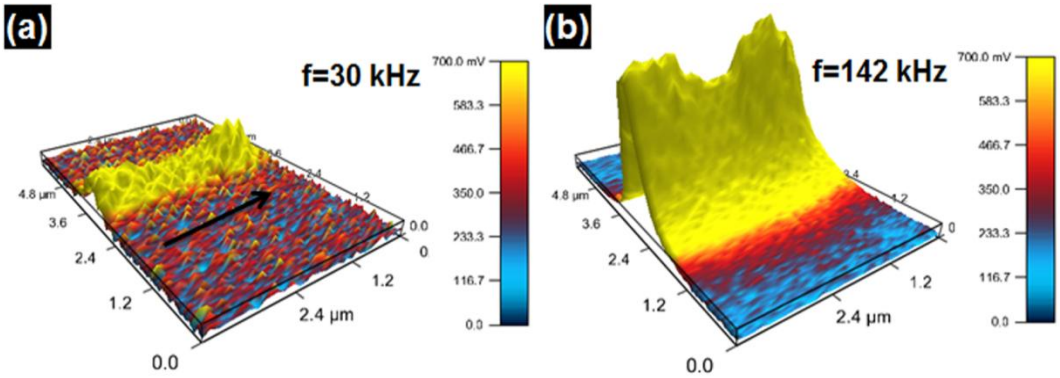

Figure S10. Expansion images from a portion of a SWNT (arrow indicates the direction along the SWNT) collected at (a) f = 30 kHz, and (b) f = 142 kHz, respectively. The same voltage (V_{ds} = 3 V) is used for the Joule heating. The z axis in both images is set at the same scale for purposes of comparison. The image at 142 kHz shows much larger signal (~11 times) than that from 30 kHz due to contact resonance enhancement.

The tip-sample interaction can be captured in a simple way with a damped harmonic oscillator model (with driving frequency of 2ω), where the amplitude of the cantilever A_c can be related to that of the surface A_s according to: [18-20]

$$A_c = A_s \frac{\omega_0'^2 - \omega_0^2}{\omega_0'^2} \frac{1}{\sqrt{(1-4\omega^2/\omega_0'^2)^2 + 4\omega^2\omega_0^2/\omega_0'^4 Q_{AFM}{}^2}} \qquad (28)$$

where w_0 and w_0' are the free resonant frequency and resonance frequency that accounts for the tip-sample interaction (ie. contact resonant frequency), respectively, and Q_{AFM} is the quality factor. When $\omega \ll \omega_0'$, then $A_c = A_s \frac{\omega_0'^2 - \omega_0^2}{\omega_0'^2} \approx A_s$. In our setups, $\omega_0' \approx 300\ kHz$, which is much larger than $\omega_0 \approx 75\ kHz$, such that the cantilever deflection is almost identical to the sample expansion in this low frequency regime. Operating at high frequency can enhance the signal, with a maximum when the heating frequency matches with the contact resonant frequency ($2\omega \approx \omega_0'$), resulting in $\frac{A_c}{A_s} \approx \frac{\omega_0'}{\omega_0} Q_{AFM}$.

7. Simulation of thermomechanical response for point defects in SWNTs

The heat transport for the SWNTs with point defects can be understood by using a 1D heat diffusion picture. Heat generated at the defect site (total power Q_{def}) will flow along the SWNT and into the surrounding materials (here is PMMA and SiO_2), as shown in figure S11a. The governing equation to solve the temperature rise $\theta(x,t)$ due to the defect heating can be written as:

$$kA\frac{\partial^2\theta(x,t)}{\partial x^2} - (1/(\frac{1}{g_{\text{int}}} + \frac{1}{g_{sur}}))\theta(x,t) = \rho CA\frac{\partial\theta(x,t)}{\partial t} \qquad (29)$$

with boundary conditions $-kA\frac{d\theta(x,t)}{dx}\Big|(x=0) = \frac{Q_{def}e^{2i\omega t}}{2}$ and $\theta\Big|(x=L) = 0$. We represent the oscillating temperature as $\theta(x,t) = \theta_0(x)\exp(2i\omega t)$, and equation (28) can be simplified as:

$$\frac{\partial^2\theta_0(x)}{\partial x^2} - \frac{1}{L_T^2}\theta_0(x) - \frac{2i}{L_D^2}\theta_0(x) = 0 \qquad (30)$$

Where $L_T = \sqrt{kA(1/g_{\text{int}} + 1/g_{sur})}$ is the thermal transfer length and $L_D = \sqrt{\frac{k}{\rho c \omega}}$ is the thermal diffusion length. Equation (30) indicates that both L_T and L_D are constrains for the heat flow along the SWNT. While both of them scales linearly with the square root of the thermal conductivity k, L_T is mainly controlled by interface thermal property and L_D is mainly controlled by frequency.

Under the experimental condition where $L_D >> L_T$ and $L >> L_T$ holds, the temperature can be approximated as:

$$\theta_0(x) = \frac{Q_{def} L_T}{2kA} e^{-x/L_T} \qquad (31)$$

This shows that the temperature along the SWNT decays exponentially from the defect site to the rest of the SWNT, with a characteristic length of L_T. Since the amount of heat flow into the PMMA is proportional to the local temperature, the shape of the expansion profile is also directly related to L_T. Finally, the temperature ratio between the defect and the rest of the SWNT is:

$$\theta_0(0) / \theta_{ave} = \frac{Q_{def}}{2L_T Q_{ave}} \qquad (32),$$

where $\theta_{ave} = Q_{ave}(1/g_{\text{int}} + 1/g_{sur})$ is the temperature of the rest of the SWNT.

Rigorous simulation of the heat transport and expansion with defects relies on the 3D FEA model (see Methods). We used two sets of parameters (Table S2), to yield similar results that match the experimental profiles quite well (Figure S11b is for the profiles along the SWNT and Figure S11c is for the cross-sections perpendicular to the SWNT). Both of the two sets of parameters yield $L_T \sim 40\,\text{nm}$. Although the temperature magnitudes are different (Figure S11d), the temperature ratio between the defect and the rest part of the SWNT are similar (ratio~13), as suggested by the simple 1D analytical model.

Table S2. Physical parameters of SWNTs and interface property

Parameter	Diameter (nm)	Thermal conductivity (W/m/K)	Thermal coupling between the SWNT and surroundings per unit area ($W/m^2/K$)
Set 1	1	700	1.5×10^8
Set 2	1	1200	4.5×10^8

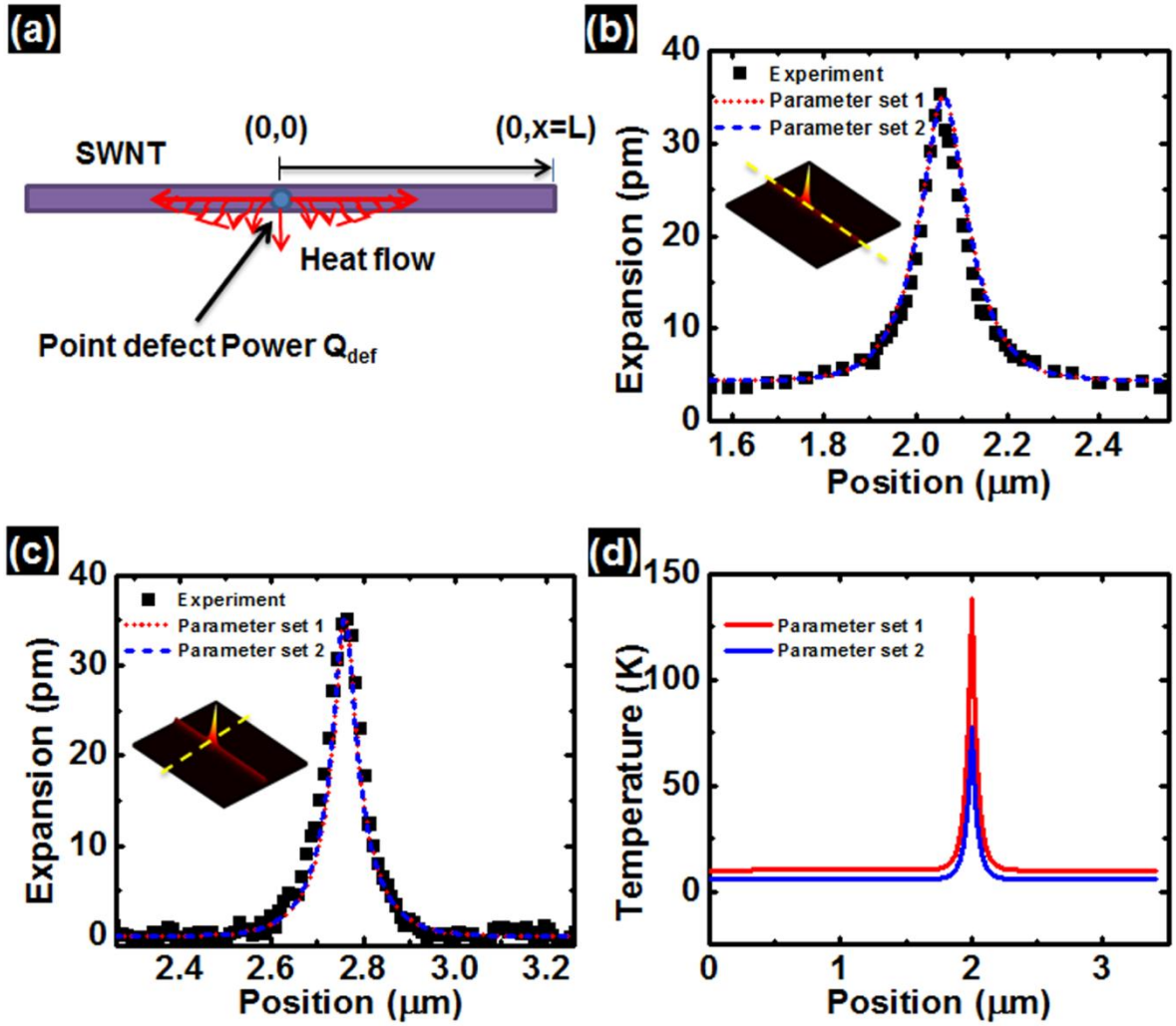

Figure S11. (a) Schematic representation of heat diffusion along the SWNT and heat flow into the surroundings. (b)-(c) Experimental (black solid square) and FEA simulated (red dotted line and blue dashed line) profiles from two sets of different parameters listed in table S2. The yellow dashed line in the inset indicates the location where the profiles are extracted. (d) Simulated temperature distribution along the SWNT for both sets of parameters.

8. Justification of the adiabatic thermal transport boundary condition used at the top surface of the PMMA

To justify the adiabatic boundary condition for the top surface of the PMMA, we calculated both convective and radiative heat losses and compared them with the total input power.

The convective heat loss from the PMMA surface can be described by $Q_C = \int h\theta_{surface} dA$,where h is the coefficient of natural convection (ranging from 5~25 $W/m^2/K$), $\theta_{surface}$ is the temperature rise at the top-surface, and A is the surface area. To do the estimation, we take a typical case shown in figure S12, where $\theta_{surface} \sim 1.5K$ for a given power density $Q_0 \sim 4W/m$. By using the upper bounds of other parameters (width of the temperature profile ~1μm and $h = 25W/m^2/K$), we can get the maximum convective heat loss per unit length along the SWNT as $\sim 3.75\times10^{-5} W/m$, which is about 5 order smaller than the input power density. For other various cases in the experiments, the temperature rise at the top-surface is typically smaller than $1K$ per $1W/m$ (input power), and width of the profile smaller than 2μm. Therefore, we conclude that the convective heat loss can be neglected in our simulations.

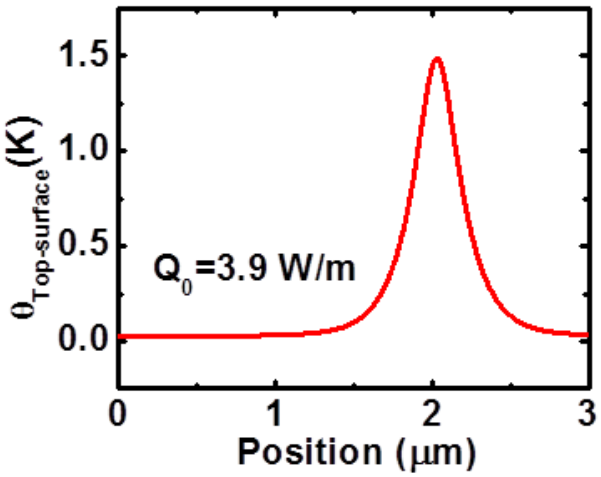

Figure S12. Temperature rise at the top surface of the PMMA, along the cross section marked by dotted lines A from figure 3b. The curve is calculated by FEA simulation, assuming an adiabatic boundary condition of heat transfer at the top surface of the PMMA.

The heat loss due to radiation can be described as $Q_R = \int \sigma[(T_0 + \theta_{surface})^4 - T_0^4]dA$,where $\sigma \sim 5.67 \times 10^{-8} W/m^2/K^4$ is the Stefan-Boltzmann constant and $T_0 = 300K$ is the ambient temperature. Again, doing estimation using $\theta_{surface} \sim 1.5K$ and width of the temperature profile ~1μm, we get the radiation loss~$9.2 \times 10^{-6} W/m$, which is also much smaller than the input power.

Supplementary References:

1. Varesi, J.; Majumdar, A. Scanning Joule Expansion Microscopy at Nanometer Scales. *Appl. Phys. Lett.* **1998**, 72, 37-39.
2. Liu, W. J.; Etessam-Yazdani, K.; Hussin, R.; Asheghi, M. Modeling and Data for Thermal Conductivity of Ultrathin Single-Crystal Soi Layers at High Temperature. *IEEE T. Electron Dev.* **2006**, 53, 1868-1876.
3. Okada, Y.; Tokumaru, Y. Precise Determination of Lattice-Parameter and Thermal-Expansion Coefficient of Silicon between 300-K and 1500-K. *J. Appl. Phys.* **1984**, 56, 314-320.
4. Tada, H.; Kumpel, A. E.; Lathrop, R. E.; Slanina, J. B.; Nieva, P.; Zavracky, P.; Miaoulis, I. N.; Wong, P. Y. Thermal Expansion Coefficient of Polycrystalline Silicon and Silicon Dioxide Thin Films at High Temperatures. *J. Appl. Phys.* **2000**, 87, 4189-4193.
5. Wortman, J. J.; Evans, R. A. Youngs Modulus Shear Modulus and Poissons Ratio in Silicon and Germanium. *J. Appl. Phys.* **1965**, 36, 153-156.
6. Ju, Y. S.; Goodson, K. E. Process-Dependent Thermal Transport Properties of Silicon-Dioxide Films Deposited Using Low-Pressure Chemical Vapor Deposition. *J. Appl. Phys.* **1999**, 85, 7130-7134.
7. Blech, I.; Cohen, U. Effects of Humidity on Stress in Thin Silicon Dioxide Films. *J. Appl. Phys.* **1982**, 53, 4202-4207.
8. Kim, M. T. Influence of Substrates on the Elastic Reaction of Films for the Microindentation Tests. *Thin Solid Films* **1996**, 283, 12-16.
9. Assael, M. J.; Botsios, S.; Gialou, K.; Metaxa, I. N. Thermal Conductivity of Polymethyl Methacrylate (Pmma) and Borosilicate Crown Glass Bk7. *Int. J. Thermophys.* **2005**, 26, 1595-1605.
10. Tsutsumi, N.; Kiyotsukuri, T. Measurement of Thermal-Diffusivity for Polymer Film by Flash Radiometry. *Appl. Phys. Lett.* **1988**, 52, 442-444.
11. Chou, S. Y.; Krauss, P. R. Imprint Lithography with Sub-10 Nm Feature Size and High Throughput. *Microelectron. Eng.* **1997**, 35, 237-240.
12. Ishiyama, C.; Higo, Y. Effects of Humidity on Young's Modulus in Poly(Methyl Methacrylate). *J. Polym. Sci. Pol. Phys.* **2002**, 40, 460-465.
13. Wu, W. L.; Vanzanten, J. H.; Orts, W. J. Film Thickness Dependent Thermal-Expansion in Ultrathin Poly(Methyl Methacrylate) Films on Silicon. *Macromolecules* **1995**, 28, 771-774.
14. Pop, E.; Mann, D. A.; Goodson, K. E.; Dai, H. J. Electrical and Thermal Transport in Metallic Single-Wall Carbon Nanotubes on Insulating Substrates. *J. Appl. Phys.* **2007**, 101, 093710.
15. Xiong, F.; Liao, A.; Pop, E. Inducing Chalcogenide Phase Change with Ultra-Narrow Carbon Nanotube Heaters. *Appl. Phys. Lett.* **2009**, 95, 243103.
16. Shi, L.; Zhou, J. H.; Kim, P.; Bachtold, A.; Majumdar, A.; McEuen, P. L. Thermal Probing of Energy Dissipation in Current-Carrying Carbon Nanotubes. *J. Appl. Phys.* **2009**, 105, 104306.
17. Liao, A.; Alizadegan, R.; Ong, Z. Y.; Dutta, S.; Xiong, F.; Hsia, K. J.; Pop, E. Thermal Dissipation and Variability in Electrical Breakdown of Carbon Nanotube Devices. *Phys. Rev. B* **2010**, 82, 205406.
18. Sarid, D., *Scanning Force Microscopy : With Applications to Electric, Magnetic, and Atomic Forces*. Oxford University Press: New York, 1991; p xi, 253 p.

19. Song, Y. X.; Bhushan, B. Atomic Force Microscopy Dynamic Modes: Modeling and Applications. *J. Phys-Condens. Mat.* **2008**, 20, 225012.
20. Gannepalli, A.; Yablon, D. G.; Tsou, A. H.; Proksch, R. Mapping Nanoscale Elasticity and Dissipation Using Dual Frequency Contact Resonance Afm. *Nanotechnology* **2011**, 22, 355705.